Journal of Geophysical Research: Earth Surface

RESEARCH ARTICLE
10.1029/2017JF004533

Morphodynamics of a Width-Variable Gravel Bed Stream: New Insights on Pool-Riffle Formation From Physical Experiments

Shawn M. Chartrand[1,2], **A. Mark Jellinek**[3], **Marwan A. Hassan**[1], **and Carles Ferrer-Boix**[4]

[1]Department of Geography, University of British Columbia, Vancouver, British Columbia, Canada, [2]Department of Earth and Environmental Sciences, Vanderbilt University, Nashville, TN, USA, [3]Department of Earth, Ocean and Atmospheric SciencesUniversity of British Columbia, Vancouver, British Columbia, Canada, [4]Department of Civil and Environmental Engineering, Technical University of Catalonia, Barcelona, Spain

Key Points:
- Changes in downstream flow velocity are spatially correlated with channel width variations
- Downstream changes in flow velocity drive width-scale bed topography adjustments
- Downstream changes in local bed slope are described by scaling theory as the net effect of two reinforcing timescales

Supporting Information:
- Supporting Information S1

Correspondence to:
S. M. Chartrand,
shawn.m.chartrand@vanderbilt.edu

Citation:
Chartrand, S. M., Jellinek, A. M., Hassan, M. A., & Ferrer-Boix, C. (2018). Morphodynamics of a width-variable gravel bed stream: New insights on pool-riffle formation from physical experiments. *Journal of Geophysical Research: Earth Surface*, *123*. https://doi.org/10.1029/2017JF004533

Received 20 OCT 2017
Accepted 21 SEP 2018
Accepted article online 27 SEP 2018

Abstract Field observations, experiments, and numerical simulations suggest that pool-riffles along gravel bed mountain streams develop due to downstream variations of channel width. Where channels narrow, pools are observed, and at locations of widening, riffles occur. Based on previous work, we hypothesize that the bed profile is coupled to downstream width variations through momentum fluxes imparted to the channel surface, which scale with downstream changes of flow velocity. We address this hypothesis with flume experiments understood through scaling theory. Our experiments produce pool-riffle like structures across average Shields stresses τ^* that are a factor 1.5–2 above the threshold mobility condition of the experimental grain size distribution. Local topographic responses are coupled to channel width changes, which drive flows to accelerate or decelerate on average, for narrowing and widening, respectively. We develop theory which explains the topography-width-velocity coupling as a ratio of two reinforcing timescales. The first timescale captures the time necessary to do work to the channel bed. The second timescale characterizes the relative time magnitude of momentum transfer from the flowing fluid to the channel bed surface. Riffle-like structures develop where the work and momentum timescales are relatively large, and pools form where the two timescales are relatively small. We show that this result helps to explain local channel bed slopes along pool-riffles for five data sets representing experimental, numerical, and natural cases, which span 2 orders of magnitude of reach-averaged slope. Additional model testing is warranted.

Plain Language Summary Mountain streams commonly display a riverbed shape that has a repetitive pattern of topographic lows and highs known respectively as pools and riffles. Visually, pools appear as relatively deep portions of a river, with slow water velocities, and riffles appear as comparatively shallow portions, with more rapid water velocities. Pool-riffles are ecologically important because salmon rely on them for birth, growth, and regeneration, and they are physically important because pool-riffles are observed across diverse landscape settings. Despite their importance, the scientific community lacks a clear explanation for pool-riffle formation. This research shows that pool-riffles develop in response to how channel width and water velocity change moving in the downstream direction. When channels narrow, pools form due to higher water velocities. When channels widen, riffles form due to lower water velocities. We demonstrate our finding with a mathematical model motivated by experimental observations and built using a combination of theory and physical scaling. The model reasonably describes pool-riffle bed topography for five different studies, representing a wide range of experimental, numerical, and natural conditions. The model can be used to test pool-riffle formation under differing conditions, and practitioners will find it useful for river restoration design purposes.

1. Introduction

Pool-riffles are a natural expression of riverbed architecture within bedload-dominated systems of gravel (2–64 mm) to cobble (64–256 mm) composition. Pools are topographic lows, related to a local tendency for net sediment particle entrainment, where local is a length scale of 1–2 reach average channel widths ($\bar{w}$). Riffles by contrast are topographic highs, reflecting the tendency for net particle deposition. Pool-riffles are observed from mountain headwaters to valley lowland settings, straight to meandering river reaches (Keller &

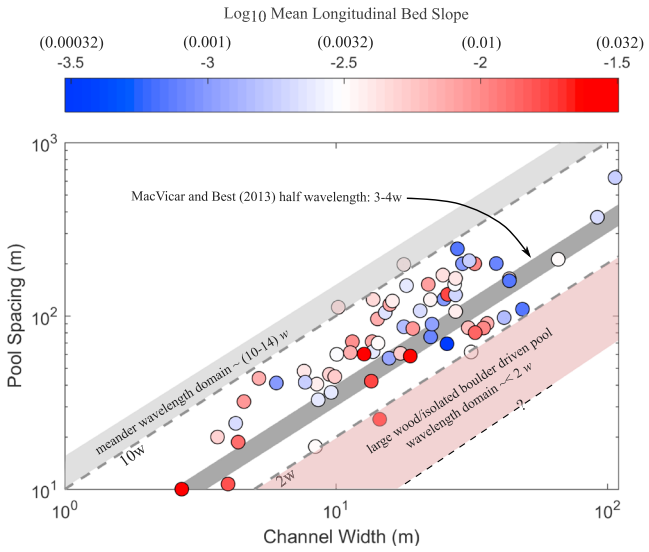

Figure 1. Downstream pool spacing as a function of the local channel width (w) for pool-riffles along relatively straight (sinuosity $\lesssim$ 1.07) and meandering reaches. Data are colored according to the log_{10} mean longitudinal bed slope. Two gray dashed lines suggest approximate limiting cases of 2 and 10$\bar{w}$; darker gray shaded area is the experimental result of (3–4)w for recovery of flow into and out of a fixed pool (MacVicar & Best, 2013), implying a pool wavelength of (6–8)w. Values in parentheses above the slope color bar are the equivalent fractional bed slope, defined as the change in bed elevation over some streamwise distance of many channel widths in length. Meander wavelength domain per Richards (1976b), and the large wood-/boulder-driven pool wavelength domain per Montgomery et al. (1995) and Beechie and Sibley (1997) are shown for reference. Plotted data from Leopold and Wolman (1957), Keller and Melhorn (1978), Montgomery et al. (1995), Sear (1996), Carling and Orr (2000), and Thompson (2001). Only straight channel data (*S*) used from Leopold and Wolman (1957), and only pool-riffle data (*PR*) used from Montgomery and Buffington (1997). The perceptually uniform *Polarmap* color map was used for slope magnitude.

Melhorn, 1978; Leopold & Wolman, 1957), and for mean longitudinal bed slopes ranging from $\approx$ 0.0001 to 0.03 (Buffington et al., 2002; Chartrand & Whiting, 2000; Church & Jones, 1982; Hassan et al., 2008; Leopold & Wolman, 1957; Leopold et al., 1964; Montgomery & Buffington, 1997). The prevalence of pool-riffles throughout river systems highlights that the necessary formative conditions are common to many different parts of the fluvial landscape. However, outside of valley lowland settings typified by sinuous or meandering river reaches (i.e., sinuosity $\gtrsim$ 1.07), we have a limited understanding of how pool-riffles form, including the underlying mechanisms.

Recent observations as well as laboratory and numerical experiments provide a framework to make progress toward addressing these knowledge gaps. Pools and riffles occur in pairs (Carling & Wood, 1994), and often in sequences of many pairs (Richards, 1976a). Measurements along natural pool-riffle sequences led to the proposal that these bed topography structures are periodically spaced, with approximate spacing $\lambda \approx 5–7\bar{w}$ (Carling & Orr, 2000; Keller & Melhorn, 1978; Leopold et al., 1964). Experimental results from MacVicar and Best (2013) agree with the pool-riffle spacing proposal. These authors observed that flow properties along a fixed-bed, experimental riffle-pool-riffle feature exhibited recovery at a length scale of 3–4$\bar{w}$, which they termed the "hydrodynamic-recovery length scale." The recovery length scale quantifies the longitudinal distance over which the flow recovers from effects related to a change in boundary geometry as flow transitions from riffle to pool (see Figures 6, 8 and 11 of MacVicar and Best (2013)). Their result implies that for similar recovery conditions over a riffle, spacing from riffle to riffle (or pool to pool) ranges from 6 to 8$\bar{w}$.

Despite the positive correlation between channel width and pool spacing, Figure 1 shows that there is considerable variance for the reported range of pool spacing (Thompson, 2013). Furthermore, pool spacing is independent of mean bed slope for the plotted pool-riffle data sets (Figure 1), despite previous results of an inverse slope dependence of riffle and pool length on mean bed slope (Wohl et al., 1993). The data trend and structure illustrated in Figure 1 supports the general idea that channel width and pool spacing are correlated and suggests that width plays a mechanistic role in pool-riffle development. However, the spread of data highlights that our present level of understanding is incomplete and also suggests that local conditions of width variation may be important.

Observation and experiments demonstrate pool colocation with channel and valley segments that are narrowing or are relatively narrow (e.g., Carling, 1991; Clifford, 1993; de Almeida & Rodríguez, 2012; Dolan et al., 1978; Lisle, 1986; MacWilliams et al., 2006; Nelson et al., 2015; Richards, 1976a; Sear, 1996; Thompson et al., 1998, 1999), and riffle colocation with segments that are widening or are relatively wide (e.g., Carling, 1991; de Almeida & Rodríguez, 2012; Nelson et al., 2015; Richards, 1976a; Sear, 1996; White et al., 2010; Wilkinson et al., 2008). Furthermore, one-, two-, and three-dimensional numerical models built to simulate specific field cases also reproduce the spatial association of pools and riffles with relatively narrow and wide channel segments, respectively (Booker et al., 2001; Cao et al., 2003; de Almeida & Rodríguez, 2011, 2012; Harrison & Keller, 2007; MacWilliams et al., 2006; Thompson et al., 1998). These combined results emphasize the anticipated coupling between downstream changes to channel width and the shape of the riverbed (Richards, 1976a), and Figure 1 raises the expectation that width change occurs over length scales of 2–10$\bar{w}$. But do pools and riffles develop in response to any magnitude of downstream width change?

Field measurements and flume experiments provide constraints on the overall width variation needed to drive pool-riffle development and maintenance (cf. Clifford, 1993). Fieldwork conducted by Lisle (1986) suggests that an obstruction that is at least 0.30$\bar{w}$ is required to develop a channel-spanning pool. By comparison, MacVicar and Roy (2007a) and Thompson and Fixler (2017) show that log structures, which effectively narrow

a channel by $\approx$ 0.40 and 0.50$\bar{w}$, respectively, lead to pool development. Thompson and McCarrick (2010) conducted flume experiments on pool development through obstruction-driven processes like that proposed by Clifford (1993), and they set the obstruction length scale as 0.40$\bar{w}$ of their experimental channel. Nelson et al. (2015) provide a systematic experimental evaluation of pool-riffle development along a variable-width setup, for which the narrowest channel location measured 0.60w of the widest section. Notably, all experiments produced bed topography resembling pool-riffles. Last, Caamaño et al. (2009) use field data and a simplified 1-D hydraulic-based criterion to show that velocity reversal from riffle to pool occurs when width reduction exceeds 30%, and flow depths over a riffle are relatively deep.

de Almeida and Rodríguez (2011, 2012) use an unsteady 1-D mixed-grain morphodynamic model to investigate pool-riffle development and evolution along a 1.1-km reach of the lower Bear River, Arkansas, USA. Their simulations show that pools readily form and were maintained in locations of channel width narrowing, and riffles form in locations of channel width widening. Streamwise reductions to channel width from riffle to pool along the simulated reach of the lower Bear River ranged from $\approx$ 0.40 to 0.50$\bar{w}$ from wide to narrow locations (de Almeida & Rodríguez, 2012). Furthermore, Carling and Wood (1994) use simulation results from a 1-D nonuniform flow model to illustrate that spatial variations of channel width similar to that reported by de Almeida and Rodríguez (2012) are necessary to drive conditions suitable for pool-riffle development and maintenance but couched within the context of a mean flow velocity reversal from riffle to pool (see; Keller, 1971).

Thompson et al. (1998), Booker et al. (2001), Cao et al. (2003), MacWilliams et al. (2006), and Harrison and Keller (2007) use two- and three-dimensional numerical models to specifically examine the fluid mechanical properties of established pool-riffle channel segments in relation to formative and maintenance hypotheses. Thompson et al. (1998), Cao et al. (2003), MacWilliams et al. (2006), and Harrison and Keller (2007) separately highlight that bulk flow acceleration into pools due to upstream wetted-width narrowing was responsible for pool formation and maintenance, which motivated the *flow convergence routing* hypothesis for pool-riffle formation and maintenance (MacWilliams et al., 2006). The flume experiments of MacVicar and Rennie (2012) and MacVicar and Best (2013) extend these numerical simulation results with observations of convectively decelerating near-bed velocities at the pool entrance along a uniform width experimental channel, but relatively rapid and large magnitude principal Reynolds stresses at the same location. The character of the principal Reynolds stresses at the pool entrance drives flow accelerations, which MacVicar and Rennie (2012) and MacVicar et al. (2013) demonstrate as a predominance of sweeps in the near-bed region, and ejections near the water surface. Sweeps in the near-bed region are thought to enhance sediment mobility (MacVicar & Rennie, 2012, and references therein) and therefore offer a direct connection with pool development.

Overall, field-based, numerical and experimental studies support the general conclusion that downstream changes to channel width beyond some threshold are sufficient to drive pool-riffle formation in a variety of landscape settings. However, important questions remain. First, what are the threshold width conditions beyond which general pool-riffle morphologies can be observed? Second, how do downstream changes to channel width physically drive pool-riffle development (and long-term persistence)? We address these two questions with basic laboratory experiments of gravel bed river morphodynamics and scaling theory, guided by three objectives. First, we develop testable theory to explain the construction of local channel bed slope as the net effect of reinforcing interaction between the timescale to do work to shape the bed, and the timescale of momentum transfer from the flowing fluid to the bed surface. Second, we characterize how bed topography and bed sediment texture conditions evolve from initial transients to steady-state conditions along an experimental channel with a downstream nonuniform width variation. Third, we use our experimental results and data from the literature to test our theory, and tentatively identify threshold width gradient conditions associated with occurrence of pool- and riffle-type structures.

We hypothesize that bed topography and sediment texture adjust to downstream patterns of flow acceleration in order to transport the upstream sediment supply. Moreover, the adjustment process and character reflects the response of a deformable gravel bed to downstream changes in channel width, and associated variations in the cross-sectionally averaged flow velocity. We further hypothesize that there is a threshold width variation (positive and negative), which is necessary to support the development of pool-riffles. The threshold conditions are associated with changes in flow velocity sufficient to drive net particle entrainment in the case of pool development, and net particle deposition in the case of riffle development. The grain size mixture characteristics of the bed surface, which reflects the relative strength of the bed, may

represent an additional factor that sets the threshold width variation conditions. Last and importantly, our work does not provide insight on the underlying mechanisms responsible for channel width variations along pool-riffle mountain streams. Local channel width variations are presumably the result of several possible mechanisms including random inputs of sediment and trees from adjacent hillslopes that locally narrow a channel, or coevolution of channel width with the local hydrodynamics, bed topography, and sediment supply. Development of natural width variations represents an important topic for future work.

2. Theory for the Local Channel Profile

The discussion in section 1 implies a six-way stress coupling between the flow, the bed, and the mobility of bed surface sediments: flow↔bed, flow↔particle, and bed↔particle (e.g., Fathel et al., 2015; Leeder, 1982). The character of this coupling depends on the momentum flux carried by the flow and is consequently sensitive to velocity variations related to changes in channel width. Particle deposition is favored at segments of channel widening where velocity decreases. Particle entrainment is favored at segments of channel narrowing where the velocity increases. The six-way coupling motivates development of a mathematical model which predicts the local channel profile.

We build from Snow and Slingerland (1987), Repetto et al. (2002), Bolla Pittaluga et al. (2014), Duró et al. (2016), Blom et al. (2016), and Ferrer-Boix et al. (2016), and begin our analysis with four assumptions: (1) a channel reach of at least $10-20\bar{w}$ in length that has a well-defined average bed surface slope; (2) statistical steady state conditions, defined as (a) bed topography adjustment rates that tend to zero across the reach and (b) comparability between the rates of total sediment supply (Q_{ss}) and sediment flux (Q_{sf}) between the upstream and downstream boundaries, respectively; (3) characteristic grain sizes of the bed surface D_i that are tending to a spatially uniform condition; and (4) channel banks that change position at rates much less than those of bed elevation and bed surface sediment texture.

We develop the channel profile model with the one-dimensional form of streambed mass conservation (Exner, 1925):

$$\frac{\partial \eta}{\partial t} = -\frac{1}{\varepsilon}\frac{\partial q_b}{\partial x}, \tag{1}$$

where $\varepsilon = (1-\phi)$ is the solid fraction in the bed, $\phi = 0.4$ is the volume-averaged streambed porosity of the active layer $L_a = kD_i$ (Hirano, 1971), k is constant between 1 and 2 (Parker, 2008), and D_i is generally taken as the D_{90} for which 90% of all particles are smaller, and q_b is the total bedload transport rate per unit channel width. Our goal is to rewrite equation (1) in terms of bed slope ($\partial\eta/\partial x$) in order to develop a predictive model. To do this, we first rewrite q_b with the dimensionless Einstein bedload number (Einstein, 1950), expressed for the sum of all bedload fractions following Parker (2007):

$$q_b^* = \frac{q_b}{(\rho' g)^{0.5} D_c^{1.5}}. \tag{2}$$

Here q_b^* is the dimensionless unit bedload transport rate, $\rho' = [(\rho_s/\rho_w) - 1]$, $\rho_s = 2{,}650$ kg/m^3 is the density of sediment, $\rho_w = 1{,}000$ kg/m^{-3} is the density of water, g is the acceleration of gravity, and D_c is a characteristic grain size. Combining equations (1) and (2) and nondimensionalizing ∂x with $\partial x \sim L_c \partial x^*$ yields

$$\frac{\partial \eta}{\partial t} \approx -\left(\frac{(\rho' g)^{0.5} D_c^{1.5}}{\varepsilon L_c}\right)\frac{\partial q_b^*}{\partial x^*}, \tag{3}$$

where L_c is a characteristic length scale we discuss below. We next introduce scales for the characteristic time T and length X of bed elevation change $\Delta\eta$:

$$\left.\begin{aligned} T &\sim \Delta\eta/(\partial\eta/\partial t), \\ X &\sim \Delta\eta/(\partial\eta/\partial x), \end{aligned}\right\} \quad \rightarrow \quad \partial t \sim \frac{T}{X}\partial x. \tag{4}$$

Applying equation (4) to the left-hand side of (3), we obtain a form of the Exner equation written in terms of bed slope:

$$\frac{\partial \eta}{\partial x} \sim -\left(\frac{(\rho' g)^{0.5} D_c^{1.5}}{\varepsilon U_c L_c}\right) \frac{\partial q_b^*}{\partial x^*}, \tag{5}$$

where U_c is a characteristic velocity scale we discuss below. $\partial q_b^*/\partial x$ is approximated as a forward finite difference over the length Δx^* with the origin at the downstream-most location:

$$\frac{\partial q_b^*}{\partial x^*} \approx \frac{q_b^*(x + \Delta x) - q_b^*(x)}{\Delta x^*}. \tag{6}$$

In addition to η, equation (5) with (2) has three unknowns: D_c, U_c, and L_c, and we require closures. Recognizing that the D_{90} has a strong influence on bed surface sediment mobility (e.g., MacKenzie & Eaton, 2017; Masteller & Finnegan, 2017; Schneider et al., 2016) and therefore local bed slope development, we take $D_c \sim D_{90f}$ with the subscript f indicating the sediment supply.

The characteristic velocity U_c reflects the rate at which a disturbance related to momentum exchange between the flow and the bed propagates downstream (e.g., Juez et al., 2016; Stecca et al., 2014, and citations therein), such as the celerity of a sediment wave. As a result, U_c is governed by the mechanical coupling of the flow to the bed, and we assume that $U_c \sim u_*$, the shear velocity. The u_* is defined as $(\tau/\rho_w)^{0.5}$, and τ is the average shear stress imparted at the bed surface. To simplify treatment of the problem, facilitate future testing by others, and have consistency with previous work (cf. Carling & Wood, 1994), we approximate τ as $\rho_w g \bar{d} S$. The variable $\bar{d}$ is the cross-sectionally averaged flow depth and S is the average local water surface slope, and we note that the energy slope was consistent with spatial trends in the water surface slope for our experiments (discussed in section 3). The uniform flow approximation of shear stress provides that $u_* = (g\bar{d}S)^{0.5}$, which assumes that d, S, and τ are averaged over a distance that is long compared to the distance over which the flow responds to spatial changes of channel geometry (cf. Paola & Mohrig, 1996). As we discuss and present below, u_* is applied locally where the assumptions concerning d, S, and τ are not strictly met, introducing a certain degree of uncertainty in calculated u_* values. Nonetheless, results are encouraging. Last, section 1 discussion suggests that $L_c \sim w$. This is a reasonable scale choice for L_c because changes in channel width drive variations in the flow velocity, which in turn scales momentum flux. Applying these closures for D_c, U_c, and L_c to equation (5) together with the approximation of $\partial q_b^*/\partial x^*$ through (6) leads to

$$\frac{\partial \eta}{\partial x} \sim -\left(\frac{(\rho' g)^{0.5} D_{90f}^{1.5}}{\varepsilon u_* w}\right) \frac{\Delta q_b^*}{\Delta x^*}. \tag{7}$$

Equation (7) can be calculated as stated to provide estimates of $\partial \eta/\partial x$. However, we want to express the problem in terms of the conditions that capture the width influence more directly. Exner (1925) assumed that the bedload transport q_b at any streamwise position in a river is proportional to the downstream flow velocity (e.g., Ancey, 2010; Paola & Voller, 2005; Slingerland & Kump, 2011). This assumption led to equation (1), and it provides a direct link between bedload transport and flow velocity. We therefore propose a scaling for the dimensionless sediment transport rate:

$$q_b^* \sim -\left(\frac{\bar{U}_x}{(\rho' g \bar{d})^{0.5}}\right), \tag{8}$$

where $\bar{U}_x$ is the cross-sectionally averaged flow velocity. Combining equation (8) with $\Delta q_b^*/\Delta x^*$, and introducing U_x^* for the nondimensional velocity term of (8),

$$\frac{\Delta q_b^*}{\Delta x^*} \sim -\Delta U_x^*. \tag{9}$$

Equation (8) is a form of Froude number $Fr = \bar{U}_x/(gL_c)^{0.5}$, the square of which expresses a balance between the kinetic energy available in the velocity field, and the potential energy stored in the bed topography. Through equation (1), the sediment transport gradient $\partial q_b/\partial x$ is a metric for the speed at which spatial differences in bedload transport propagate along the system as a profile disturbance. Our scaling assumes that profile disturbances propagate at a wave speed that scales as spatial differences in $\bar{U}_x$. Positive differences of $\bar{U}_x$ drive profile changes upstream to downstream, and negative differences vice versa. ΔU_x^* is evaluated with the origin at the downstream most location as

$$\Delta U_x^* = U_x^*(x + \Delta x) - U_x^*(x). \tag{10}$$

Last, substituting equation (9) into (7), we obtain the final form of our mathematical model for the local bed slope, $\partial\eta/\partial x \equiv S_{\text{local}}$:

$$S_{\text{local}} \sim \Lambda\left(\Delta \bar{U}_x^*\right), \tag{11}$$

where

$$\Lambda = \frac{(\rho' g)^{0.5} D_{90f}^{1.5}}{\varepsilon w u_*}. \tag{12}$$

Λ characterizes development of the local channel profile in terms of reinforcing interaction between the timescale over which turbulent stresses acting at the scale of D_{90} are imparted at the deformable bed, and the timescale for bed yielding through particle entrainment and/or deposition. To explicitly express this underlying dynamic, we expand equation (12):

$$\Lambda = \underbrace{\left(\frac{[\rho' g D_{90f}]^{0.5}}{\varepsilon w}\right)}_{1/t_y}\underbrace{\left(\frac{D_{90f}}{u_*}\right)}_{t_f} = \frac{t_f}{t_y}. \tag{13}$$

Here t_f is the flow time and t_y is the yielding time. The flow time is interpreted as the timescale for the delivery of momentum flux to the bed (cf. Carling & Orr, 2000; Yalin, 1971), which is set by the magnitude of the shear velocity u_*. As a result, t_f scales the resultant dynamic pressure force imparted at the bed surface and the D_{90f}, for the assumed statistical steady state conditions. The flow time ratio t_f (13) indicates that larger shear velocities yield smaller relative flow timescales, and smaller shear velocities yield larger flow timescales.

The yielding time is interpreted as the timescale for entrainment of sediment particles resting on the bed surface, which is set by the relative mass (i.e., size) of the D_{90f}, the packing condition of the bed surface sediments ε and the local channel width w. As a result, t_y scales the relative time to do work to the full width of the channel bed. The yielding time ratio $1/t_y$ (13) indicates that for the simplest case of a uniform packing condition, larger widths have larger relative yielding timescales, and smaller widths have smaller yielding timescales.

However, the packing condition or relative bed strength ε is also important in setting t_y. Assuming D_{90f}, w and t_f are steady at any particular location, if the bed weakens and $\varepsilon \to 0$, $t_y \to 0$ and the bed deforms through particle entrainment. An example of this is removal of the surface armor layer followed by a rapid increase in the rate of particle entrainment (e.g., Wang & Liu, 2009). On the other hand, if the bed strengthens and $\varepsilon \to 1$, $t_y \gg 0$ and bed elevation is approximately steady, or the bed deforms through particle deposition. An example of this is development of surface sediment structures and the associated reduction of net local transport rates (e.g., Church et al., 1998). We provide further support for our treatment of equation (13) by independently recovering t_y through the following scaling: $(\rho_w w^2/t_y^2) \sim (\Delta\rho g D_{90}/\varepsilon^2)$ where the left-hand side scales the yield stress τ_y of the bed, the right-hand side scales the relative bed strength (analogous to the denominator of the Shields equation; Shields, 1936), $\Delta\rho = \rho_s - \rho_w$, and ε^2 is a function of surface area. Simplifying yields, $(1/t_y) \sim ([\rho' g D_{90}]^{0.5}/\varepsilon w)$.

There are three critical take away points from the derivation of equation (11) and the discussion of Λ. First, (11) was derived assuming steady state conditions. Therefore, t_y and t_f are understood as characteristic timescales for any particular streamwise location following relaxation from a local disturbance to a roughly steady condition. A change of channel width is one example of a local disturbance. Second, the sign of S_{local} is determined by how downstream changes of $\bar{U}_x$ and $\bar{d}$ compare. Third, S_{local} is determined by how $1/t_y$ compares to t_f, rather than the magnitude of either quantity alone. This is particularly important because section 1 discussion implies that u_* covaries with w. At wide segments, or riffles, u_* is relatively low, and at narrow segments, or pools, u_* is relatively high, consistent with previous field and simulation results (see; Carling, 1991; Carling & Wood, 1994; MacVicar & Roy, 2007a; MacWilliams et al., 2006, for detailed discussions of u_* and τ variation within pool-riffles). The magnitude of Λ variation between riffle and pool therefore depends on how specifically width and shear velocity covary, which in turn sets up the morphodynamic reinforcement between the associated timescales t_y and t_f. For example, equation (13) and the discussion of section 1 suggest that at wide segments, t_y and t_f are both relatively large, promoting sediment deposition, and at narrow segments each

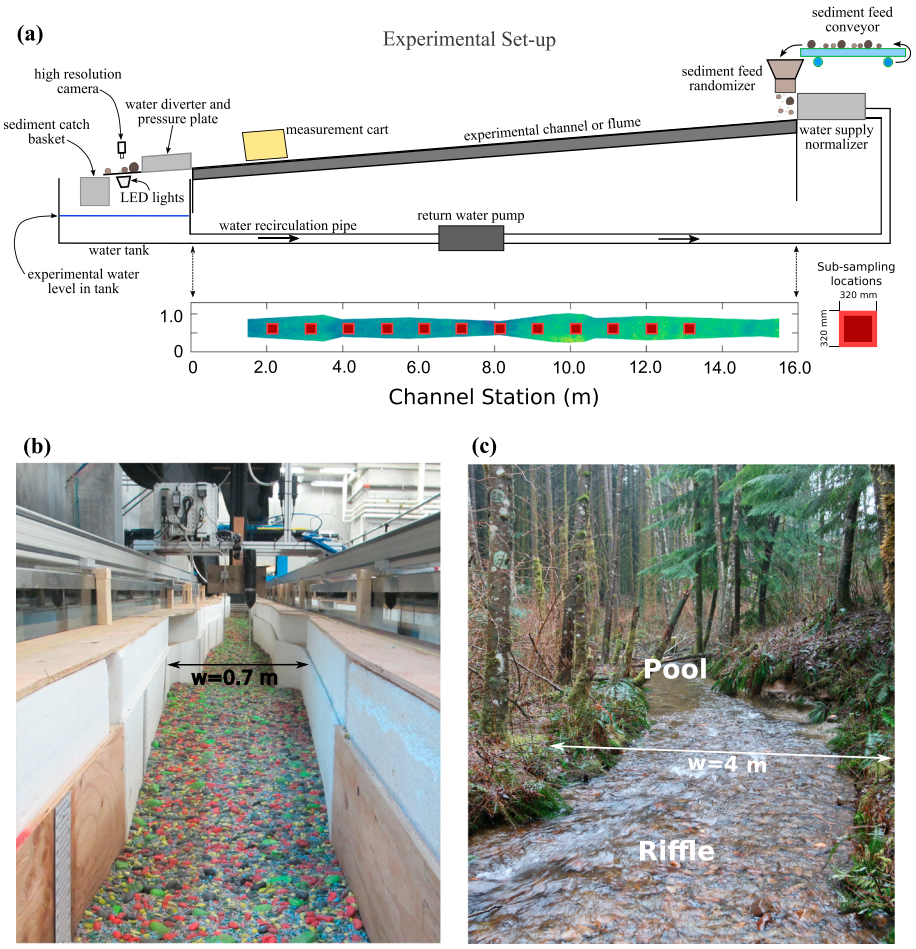

Figure 2. Overview and images of the experimental setup and field stream reach. (a) Schematic illustration of the of the experimental setup, including an overhead view of the experimental channel, showing the downstream width variation and subsampling locations indicated by red boxes. (b) Photograph of the experimental channel. The photograph view is looking upstream from station 1,000 mm. Photograph taken at experimental time 2,150 min. (c) Photograph of the field channel East Creek. The photograph view is looking downstream at a typical pool-riffle pair. Average channel width narrows by approximately 25% from riffle to pool.

timescale is relatively small, promoting sediment entrainment. We test equation (11) and proposed links to pool-riffle morphology through experimental data and discuss the results in sections 5 and 6.1.

3. Laboratory Experiment and Methods

3.1. Setup

Pool-riffle experiment 1 (PRE1) was conducted at the BioGeoMorphic eXperimental Laboratory at the University of British Columbia, Vancouver, Canada (Figures 2a and 2b). The experimental flume is 15 m long and 1 m wide. Water is recirculated using a pump (Figure 2) and enters the flume at the upstream boundary through a series of stacked 0.05-m ∅ plastic pipes collectively called the "flow normalizer." The normalizer is used to reduce vorticity introduced within the flume head tank. Sediment is introduced to the flume via a speed-controlled conveyor, which dumps particles into a mixing chamber we call the "randomizer." As particles fall through the mixing chamber, their pathways are interrupted by the crossbars, which flings the particles along random trajectories, providing a spatially random distribution of sediment fall points on the inlet flume bed. The randomizer action provides a spatially and temporally uniform inlet boundary condition.

Sediment exits the flume through a uniform width channel section that measures 1 m long. We use this outlet configuration to control the hydrodynamic conditions of the water and sediment, which ultimately passes through a particle imaging light box (Figure 2a; cf. Zimmermann et al., 2008a, for light table

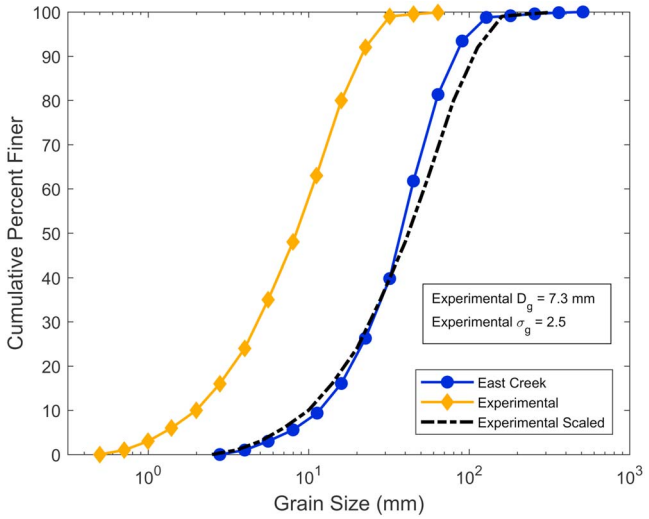

Figure 3. Cumulative grain size distribution for the experiment and the field reach along East Creek, with grain size in millimeters shown on the *x* axis, and cumulative percent finer on the *y* axis. The experimental distribution was scaled according to the geometric ratio $L_r = 5$.

description). Figures 2a and 2b show that the experimental channel consists of downstream varying channel width. Width variations reflect the average downstream changes between inflection points along a field site (discussed next). We impose the experimental width conditions by constructing a channel inside the flume with rough-faced veneer-grade D plywood, which has a surface roughness that varies from 1 to 4 mm, or roughly 0.15 to 0.60 times the geometric mean grain size of the experimental grain size mixture (discussed next). The experiments were developed to explicitly test how downstream changes to channel width affect bed slope development. As a result, channel wall heights were constructed to contain all experimental flows.

The experimental setup provides a basic representation of morphodynamics along relatively straight gravel bed mountain stream reaches, which exhibit downstream variations of channel width. However, it is important to point out that the experimental setup does not provide the conditions necessary to support all morphodynamic feedbacks that ultimately set the shape and character of natural mountain stream beds and planform configurations. For example, the experimental setup does not allow for bank erosion, and the consequent interplay between bank erosion and bed topography response in the downstream and cross-stream dimensions (e.g., Eaton et al., 2006). Second, downstream symmetry of the experimental channel width variations along the centerline suppresses relatively large differences in local cross-stream sediment transport rates. This has implications for how the experimental bed evolves and responds to upstream variations of flow and sediment supply, which likely do not capture important pool-riffle maintenance dynamics reported for natural streams where pool-riffle features are offset from the channel center (Bayat et al., 2017).

3.2. Experimental Design

The experimental design was guided by a 75-m-long reach of East Creek, University of British Columbia Malcolm Knapp Research Forest. East Creek is a small gravel bedded mountain stream (Figure 2c). The field reach was chosen because it exhibits pool-riffles and roughened-bed channel segments, with a reach-averaged bed slope $S_b = 0.015$. Roughened-bed channel segments are characterized by local bed topographies with variations that scale as a few multiples of the bed surface D_{90} and visually appear as a randomly sorted coarse bed surface. Following Henderson (1966), the geometric scale ratio for the experimental channel is $L_r = 5$, where the subscript *r* indicates the field:model length ratio.

The experimental channel width and grain size distribution were calculated from L_r (Figures 2 and 3), and the experimental channel slope equals that of the field site. The minimum width along the experimental channel is 0.370 m (station 8.150 m), and maximum width is 0.785 m (station 9.960 m). This gives a maximum to minimum width ratio of ≈2.1. Width variations provide a range of downstream width gradients from (−0.26) to (+0.47). The model grain size distribution ranges from 0.5 to 32 mm, with a geometric mean size of 7.3 mm (D_g), a D_{90} of 21.3 mm, and a geometric standard deviation of 2.5 (σ_g; Figure 3). Each grain size fraction was painted a unique color to aid with image-based analysis of the surface grain size distribution (see supporting information S1 for details).

We applied conventional Froude scaling to determine the water supply flow rates for our experiments, which requires Fr_r=1 (e.g., Henderson, 1966), where Fr_r is the Froude number field:model ratio. We rearrange Fr_r and solve for the field:model velocity ratio, yielding $\bar{U}_{x,r}=(g_r L_r)^{0.5} \propto L_r^{0.5}$. $\bar{U}_{x,r}$ provides a link to the geometric scaling of the experiment, and the basis of experimental flow scaling: $Q_r=\bar{U}_{x,r}L_r^2 \propto L_r^{2.5}$, where Q_r is the flow discharge field:model ratio. The field estimate of bankfull flow is 2.3 to 2.5 m^3/s, and the associated experimental flow Q_w based on Q_r is 42 liters per second (L/s). Two higher flows of 60 and 80 L/s were also used (Table 1) and equate to flood magnitudes of roughly 5- and 10-year recurrence intervals, respectively.

PRE1 flow magnitudes were sufficient to transport the full experimental grain size distribution and are characterized by average τ/τ_{ref} values, which approach 2.0 (Table 1; Wilcock & McArdell, 1997). τ_{ref} is the reference critical mobility stress for the bed surface median particle diameter D_{50}, calculated according to

Table 1
Experimental Details for PRE1

PRE1 interval	t_o	t_e	Q_w	Q_{ss}	Q_{sf}	η'	D'_g	D'_{90}	τ/τ_{ref}	DEM/photo
(-)	(-)	(min)	(L/s)	(kg/min)	(kg/min)	(-)	(-)	(-)	(-)	(-)
0	0	0	—	—	—	0.90	0.842	0.820	—	yes
1	0.2	19	42	0.50	0.009	0.88	0.985	0.983	1.49	yes
2	0.5	50	42	0.50	0.027	0.88	1.170	1.013	1.47	yes
3	1.0	110	42	0.50	0.064	0.89	1.134	1.009	1.48	yes
4	2.1	230	42	0.50	0.048	0.90	1.164	1.008	1.44	yes
5	4.3	470	42	0.50	0.027	0.94	1.183	0.996	1.53	yes
6	6.5	710	42	0.50	0.050	0.97	1.208	0.925	1.59	yes
7	8.6	950	42	0.50	0.030	0.97	1.233	0.974	1.54	yes
8	10.8	1,190	42	0.50	0.016	1.01	1.214	1.003	1.57	yes
9	13.0	1,430	42	0.50	0.099	1.06	1.299	1.012	1.54	yes
10a	15.2	1,670	42	0.50	0.058	1.10	1.209	0.985	1.63	yes
10b	16.3	1,790	42	0.50	0.660	—	—	—	—	no
11a	17.4	1,910	42	0.50	0.437	1.07	1.149	0.994	1.56	yes
11b	18.5	2,030	42	0.50	0.226	—	—	—	—	no
12[a]	19.5	2,150	42	0.50	0.393	1.09	1.202	1.059	1.56	yes
13a	19.8	2,180	60	0.80	4.284	—	—	—	—	no
13b	20	2,195	60	0.80	7.113	—	—	—	—	no
13c	20.2	2,225	60	0.80	3.670	1.01	0.991	1.052	1.75	yes
14a	20.6	2,270	60	0.80	2.296	—	—	—	—	no
14b[a]	21.7	2,390	60	0.80	0.917	0.98	1.143	1.146	1.66	yes
15a	21.9	2,405	80	1.00	3.848	—	—	—	—	no
15b	22.1	2,429	80	1.00	3.840	—	—	—	—	no
15c	22.3	2,450	80	1.00	3.303	0.96	1.102	1.185	2.00	yes
16a	22.5	2,480	80	1.00	2.554	—	—	—	—	no
16b	23	2,525	80	1.00	1.336	—	—	—	—	no
16c[a]	23.4	2,570	80	1.00	0.927	0.94	1.294	1.198	1.78	yes
17	23.9	2,630	80	1.00	1.067	0.94	1.302	1.219	1.77	yes
18	26.1	2,870	42	0.50	0.033	0.96	1.330	1.190	1.26	yes
19	28.3	3,110	42	0.50	0.016	1.00	1.309	1.126	1.45	yes
20	30.5	3,350	42	0.50	0.013	1.04	1.306	1.101	1.52	yes
21	32.6	3,590	42	0.50	0.018	1.08	1.352	1.100	1.50	yes
22	34.8	3,830	42	0.50	0.022	1.12	1.330	1.063	1.64	yes
23	37	4,070	42	0.50	0.143	1.15	1.248	1.032	1.66	yes
24[a]	39.2	4,310	42	0.50	0.509	1.14	1.132	0.999	1.68	yes
25a	39.4	4,336	60	0.80	4.488	—	—	—	—	no
25b	39.6	4,351	60	0.80	9.622	—	—	—	—	no
25c	39.7	4,370	60	0.80	5.479	—	—	—	—	no
25d	39.9	4,385	60	0.80	4.527	1.04	1.131	1.170	1.71	yes
26a	40.3	4,430	60	0.80	2.436	—	—	—	—	no
26b[a]	41.4	4,550	60	0.80	0.595	1.03	1.225	1.171	1.62	yes
27a	41.5	4,565	80	1.00	2.231	—	—	—	—	no
27b	41.7	4,589	80	1.00	6.212	—	—	—	—	no
27c	41.9	4,610	80	1.00	5.062	0.96	1.082	1.210	1.75	yes
28a	42.2	4,640	80	1.00	2.069	—	—	—	—	no
28b	42.6	4,685	80	1.00	1.132	—	—	—	—	no
28c	43	4,730	80	1.00	0.892	0.97	1.374	1.195	1.91	yes
29	43.5	4,790	80	1.00	0.600	0.97	1.358	1.242	1.74	yes

Note. The elapsed time indicates the end time for the specified experimental interval. The repeat phase of PRE1 began at elapsed time 2,630 min. Relevant quantities averaged over the 12 subsmapling locations.
[a]Achievement of mass comparability between feed and flux.

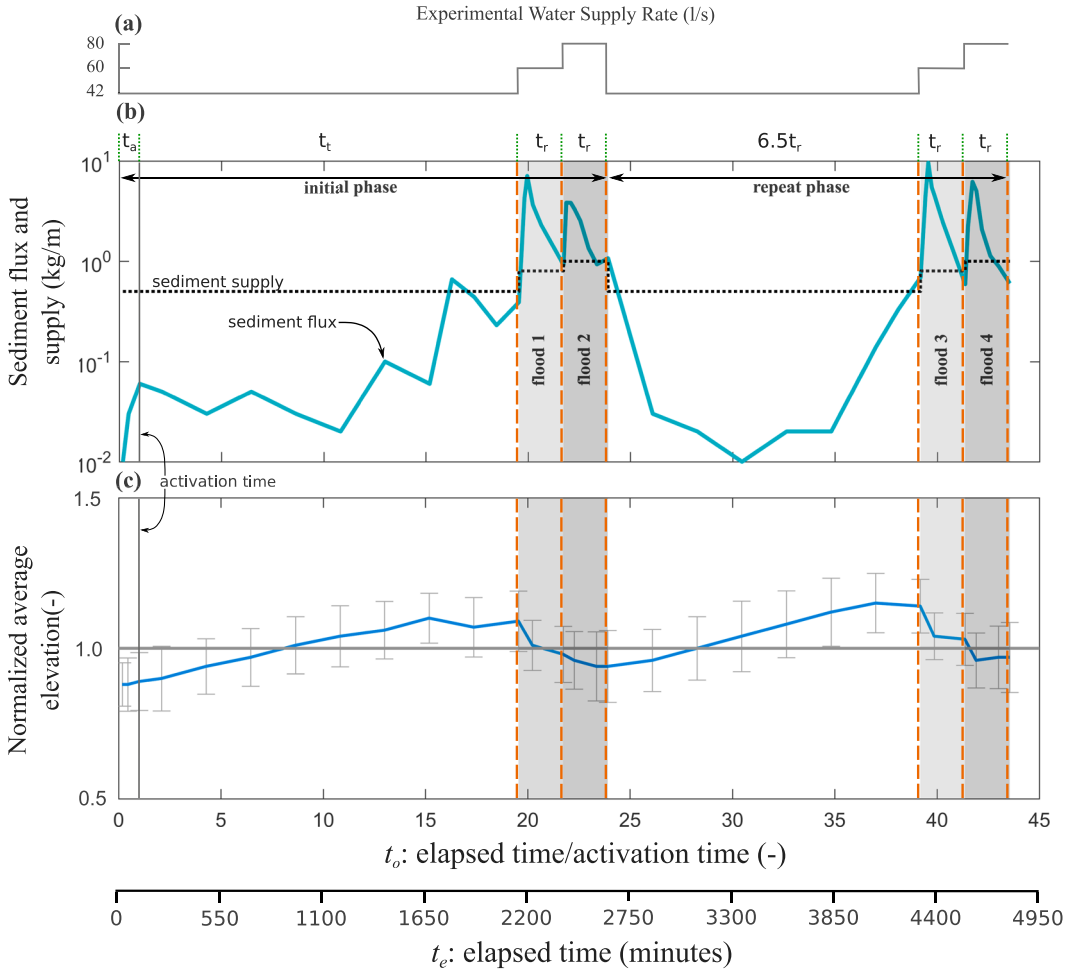

Figure 4. PRE1 experimental summary: water, sediment supply, and sediment flux (measured at flume outlet) and normalized longitudinal mean bed topography versus the dimensionless time t_o. (a) Water supply rate (Q_w; L/s). (b) Sediment supply rate and flux (Q_{ss} and Q_{sf}, respectively; kg/min). (c) Normalized longitudinal mean bed topography ($\bar{\eta}'$), calculated as the ratio of the time-specific mean bed elevation for all subsampling locations, to the mean bed elevation across all subsampling locations and observation times. Error bars represent one standard deviation about the mean. Activation (t_a), transient (t_t), and response (t_r) periods indicated at the top of (b); steady state indicated by vertical dashed lines in (b) and (c) and discussed within section 4.1.

Shields (1936) as

$$\tau_{\text{ref}} = \tau^*_{c_{50}}(\rho_s - \rho_w)gD_{50} \tag{14}$$

where $\tau^*_{c_{50}}$ is the dimensionless critical stress for the D_{50}. We calculated the reference critical mobility stress for $\tau^*_{c_{50}} \approx 0.035$ (here forward τ^*_{ref}). This value for τ^*_{ref} is consistent with empirical mobility conditions of a sand-gravel mixture with a bulk sand content of about 10% (Wilcock & Crowe, 2003), which matches the PRE1 distribution (Figure 3). In addition, results and findings reported here do not explicitly depend on the chosen value of τ^*_{ref}, because we are primarily concerned with spatial trends of sediment mobility, as opposed to any particular value along the experimental channel. Last and as a point of reference, experimental flows were characterized by Reynolds number $Re \gtrsim 10^5$. The Reynolds number for fully developed and hydrostatic flows is defined as $Re=(Q_w\bar{d})/(A\nu)$, $A=\bar{d}w$ is the flow area, and ν is the kinematic viscosity of water. Experimental water temperature was approximately 15 °C.

We chose Q_{ss} through numerical simulations following Parker (2007) and Ferrer-Boix and Hassan (2014), as well as trial experiments. Selected values of Q_{ss} for each flow are 0.5, 0.80, and 1.0 kg/min, respectively (Table 1), and represent an approximation of the flume-wide average theoretical transport capacity. Averaging was necessary due to the variable width condition of the experimental setup.

3.3. Experimental Procedure and Data

We began PRE1 with a relatively flat bed and a uniform slope. Prior to smoothing, the full thickness of sediment in the flume was thoroughly mixed to establish a random size distribution, and to remove textural heterogeneity related to previous trial runs (Figure 2b). Figure 4 shows Q_w in liters per second versus time in minutes (a), and Q_{ss} in kg/min (b). PRE1 consisted of an initial and repeat phase (Figure 4b). The initial phase extends from $t_e = 0–2{,}630$ min ($t_o = 0–23.9$), and the repeat phase extends from $t_e = 2{,}630–4{,}790$ min ($t_o = 23.9–43.5$), where t_e is elapsed time (t_o is nondimensional time discussed in section 4.1; Table 1 and Figure 4b).

Flow and sediment supply continued at constant values until spatially averaged bed topography was steady, total sediment flux approximated the sediment supply rate, and the fractional flux was comparable to the fractional supply determined by a two-sample Kolmogorov-Smirnov test (Massey, 1951). We used a ramping up and down period of 4–5 min each time the water supply was raised and lowered to and from the experimental flows in order to minimize disturbance to the established bed topography and surficial grain size sorting conditions. The repeat phase began from the prevailing channel topographic and bed surface sediment sorting conditions established by the end of the initial phase. The processed experimental data used in this paper can be freely accessed through an online data repository (Chartrand et al., 2017).

4. Results

4.1. General Experimental Response Regimes

We identify four bed topographic and surface sediment texture response regimes for PRE1 (i.e., morphodynamics; Figure 4). The first response regime occurs during the activation time t_a. The *activation time* is the timescale over which the initial bed topography and sediment texture along the experimental channel respond to an imposed change to the upstream boundary conditions (Figure 4b). We use 110 min for the PRE1 activation time to normalize the elapsed time t_e. The time $t_o = (t_e/t_a)$ consequently characterizes PRE1 morphodynamics in terms of the time to communicate a boundary condition change through the entire experimental channel. Activation time occurs from $t_o = 0–1$. The second response regime is the transient time t_t. The transient time is the period over which the flow develops toward a statistical steady condition in response to evolving spatial patterns of channel bed topography and sediment texture. The transient time occurs from $t_o = 1–19.5$. The third response regime is the steady state (SS). At the start of section 2 and in the context of our experiments, steady state is defined by $\partial\bar{\eta}/\partial t \rightarrow 0$, $Q_{sf} \approx Q_{ss}$ and $\partial D_i/\partial x \rightarrow 0$. Six separate steady states were approached or occurred at $t_o = 19.5$, 21.7, 23.9, 39.2, 41.4, and 43.5. The fourth response regime is the steady state response time t_r. The response time is the period over which bed topography and sediment texture evolve to new SS conditions due to a change of the upstream water and sediment supplies. There are five separate steady state response periods from $t_o = 19.5–43.5$ for PRE1. Four of these response periods are of similar duration, whereas the fifth is about 6.5 times longer (Figure 4b). These four response regimes are used to present the main experimental results.

4.2. Experimental Evolution of Sediment Flux, Mean Bed Topography, and Characteristic Grain Sizes

Overall, Q_{sf} and η' each show similar responses between the initial and repeat phases and vary systematically in relation to the upstream supplies, where $'$ indicates normalization of η by the reach average elevation (Figures 4b and 4c). Q_{sf} increases to a peak during t_a before abruptly changing, whereas η' exhibits a small positive rate of change. During the t_t, Q_{sf} remains relatively low and consistent until $t_o = 15.2$, after which Q_{sf} increases to the supply rate and fluctuates around Q_{ss} through the end of the t_t (Figure 4b). The $\bar{\eta}'$ on the other hand increases at a uniform rate during the t_t until $t_o = 15.2$, indicating a buildup of sediment storage. After $t_o = 15.2$, $\bar{\eta}'$ was approximately steady (Figure 4c). When the rate of bed topography adjustment approaches 0, Q_{sf} increases to match Q_{ss}. Stepped increases in supply during the t_r periods of floods 1, 2, 3, and 4 cause an evacuation of stored sediment from the experimental channel, decreases of $\bar{\eta}'$, and associated increases of Q_{sf} to peaks (Figures 4b and 4c). Following Q_{sf} peaks, sediment flux decreases to match Q_{ss}. The t_r period of the repeat phase from $t_o = 23.9–39.2$ exhibits a sediment storage accumulation trend similar to that of the t_t during the initial phase (Figure 4c). However, Q_{sf} shows a relaxation away from the perturbation of flood 2 from $t_r = 23.9–30.5$, even while sediment storage increases (Figure 4b).

Apart from the coarsening signals at x4000 and x6000 during the repeat phase, the relative magnitude of normalized D_g' responses are generally similar between the initial and repeat phases, and the mean value systematically varies across PRE1 (Figure 5b). Following $t_o = 0.5$, the mean D_g' attains a value of 1.17 and fluctuates around a value of 1.2 as sediment storage builds through t_a and most of t_t until $t_o = 19.5$ (Table 1 and Figure 5b). Stepped increases in water and sediment supply at the start of flood 1 t_r results in fining of

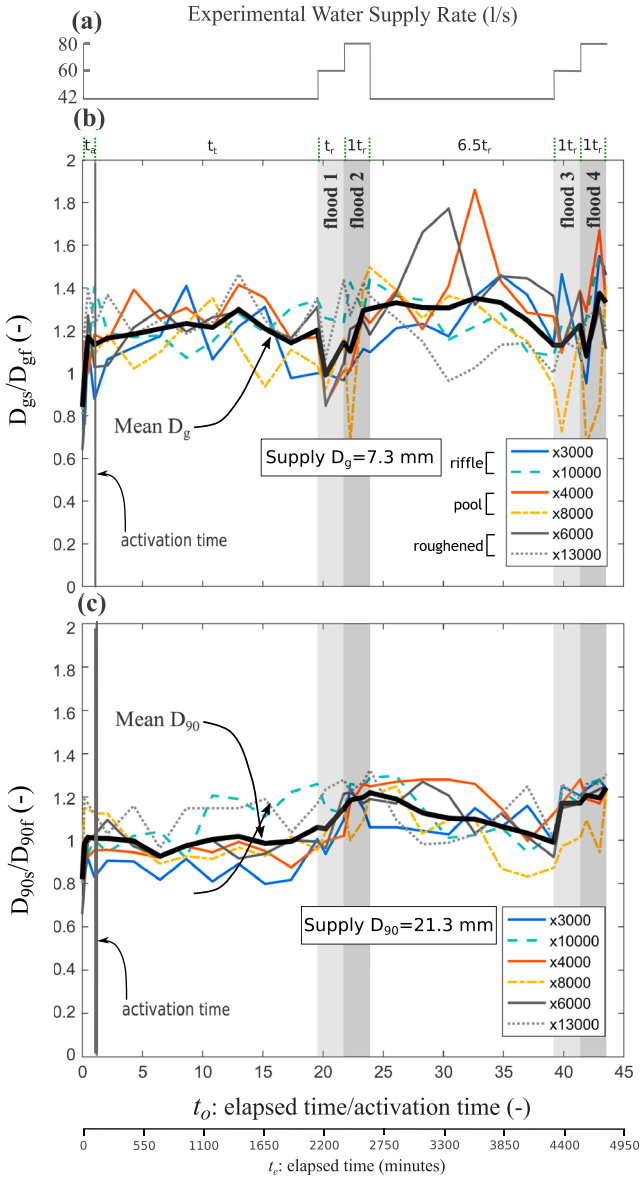

Figure 5. PRE1 experimental summary: water supply, D_g and D_{90} grain sizes versus the dimensionless time t_o. (a) Water supply rate (Q_w; L/s). (b) Normalized D'_g grain size, calculated as the ratio of the bed surface D_{gs} to the supply D_{gf} (supply D_{gf} = 7.3 mm). (c) Normalized D'_{90} grain size, calculated as the ratio of the bed surface D_{90s} to the supply D_{90f} (D_{90f} = 21.3 mm). Heavy black lines in (b) and (c) are the mean responses for all locations shown. Activation (t_a), transient (t_t), and response (t_r) periods indicated at the top of (b) and discussed within section 4.1.

the mean D'_g to a value of 0.991, representing a 30% fining response. Following the initial fining, D'_g coarsens during the t_r periods of floods 1 and 2 to a value of 1.30 at the end of the initial phase, or 30% coarser than the sediment supply D_g (t_o = 23.9). From the beginning of the repeat phase and the third t_r period to t_o = 34.8, the mean D'_g was steady and then declines to a value of 1.13 at t_o = 39.2. During the t_r periods of floods 3 and 4, the mean D'_g fluctuates by about 30%, and at the end of PRE1 has a value of 1.35, or 35% coarser than the sediment supply D_g (Table 1 and Figure 5b). D'_g adjustments between pool, riffle, and roughened channel segments do not show clear feature-specific trends across PRE1 (identification of these structures is discussed in section 4.3). However, one trend occurs during all four floods and associated t_r periods. The riffle at station 10 m was generally coarser than the pool at station 8 m (Figure 5b) during evolution to SS. However, at SS the pool and riffle were of comparable texture. Texturally, the riffle D'_g was 10–50% coarser than the pool during evolution to SS. Compared to the sediment supply D_g, the riffle was coarser, and the pool was finer during these times.

The normalized D'_{90} has trends through PRE1 which are generally similar to those of D'_g, and the mean value systematically varies across PRE1 (Figure 5c). Following t_o = 0.5, the mean D'_{90} attains a value of approximately 1 and this value persists as sediment storage builds through t_a and most of t_t until t_o = 19.5 (Table 1 and Figure 5c). Stepped increases in water and sediment supply with floods 1 and 2 results in coarsening of the mean D'_{90} through both associated t_r periods. By the end of the initial phase at t_o = 23.9, the mean D'_{90} had a value of 1.19, or 19% coarser than the sediment supply D_{90}. From the beginning of the repeat phase to t_o = 39.2, the mean D'_{90} declines to a value of 0.99 (Table 1 and Figure 5c). D'_{90} rises when flow and sediment supplies increase at the start of flood 3 and increases from then on to the end of PRE1 with a final value of 1.24, or 24% coarser than the sediment supply D_{90}. Similar to the D'_g, D'_{90} adjustments between pool, riffle, and roughened channel segments do not show clear feature-specific trends across PRE1. However, during the t_t period and all four floods of PRE1, the riffle at station 10 m was generally coarser than the pool at station 8 m (Figure 5c). Texturally, the riffle D'_{90} was 10–25% coarser than the pool during these times. Compared to the sediment supply D_{90}, the riffle was commonly coarser and comparable to, and the pool comparable to, and finer than the supply. The contrasts of sediment texture between riffle and pool are commonly reported field trends (cf. Hodge et al., 2012; Lisle, 1979). However, similar to the results for D_g, pool D_{90} texture was also comparable to riffle texture toward the end of the initial and repeat flood sequences (Figure 5c). This result is supported by Milan (2000), for example, who reports that pools were coarser than riffles at the River Rede, Northumberland, UK, study reach during the time period of that study.

4.3. Topographic Response: Channel-Wide and Longitudinal Profile Development

Figure 6 provides a record of channel bed topography evolution during PRE1, for the times t_a through the early part of t_t. Stations within segments of strong widening and narrowing, for example, 10 and 8 m, respectively (Table 2), display rapid topographic development during t_a (Figure 5). During the same time Q_{sf} increases to a peak value of 0.064 kg/min (Figure 4 and Table 1). At station 8 m, channel width has the strongest negative downstream width difference: $\Delta w(x) = -0.25$ (Table 2), and here the width reduction correlates with a local topographic low. By the end of the t_a (t_e = 110 min), this topographic low is well developed.

Width increases at 10 and 3.6 m correlate with topographic highs, and the initial style of topographic construction at these two stations differs during the t_a (Figure 6). At the downstream location, topography builds

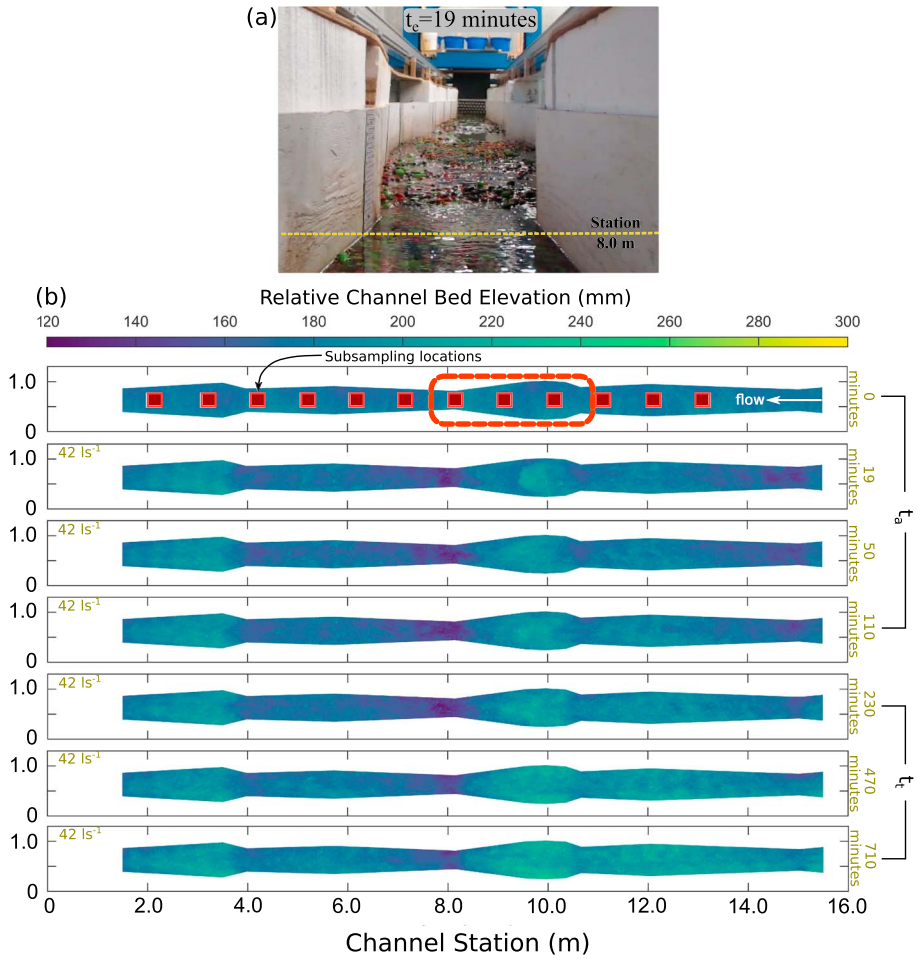

Figure 6. Photograph of experimental condition for PRE1 and summary panel of topographic responses observed during t_a and the early part of t_t. Panel (a) shows experimental bed conditions for t_e = 19 min looking upstream from station 7.8 m. The yellow dashed line indicates station 8 m for reference, and the deposit location evident in the image center occurs from approximately station 9–10.5 m. Photograph main field of view depicted by the red circled region in the topographic panel for t_e = 0 min. Photograph captured with flow of approximately 3.0 L/s. Panel (b) shows topographic responses for t_e = 0, 19, 50, 110, 230, 470, and 710 mins. At the side of each DEM we provide the elapsed time, and within each DEM we indicate the flow rate for the preceding experimental interval.

via progressive deposition of sediments over the entire riffle surface. At the upstream location, by contrast, topography builds by migrating fronts of bedload sediment. Each location corresponds to relatively large positive downstream width changes: $\Delta w(x)$ = 0.19 and 0.17, respectively (Table 2). Channel segments for which $\Delta w(x) = O(0)$ (Table 2) exhibit muted topographic responses during the t_a, relative to the narrow and wide zones. Topographic response differences between stations 10 and 3.6 m diminish by the start of the t_t, and topographic construction continues at both stations by incremental deposition of bedload. Subtle topographic development also continues at channel segments for which $\Delta w(x) = O(0)$. By t_e = 230 min, the spatial pattern of bed topography downstream of station 10.6 m is established. Upstream of this location and after t_e = 230 min, bed topography continues to build through t_e = 710 min (Figure 6).

Figure 7 provides a record of steady state topography for PRE1. For all six SS conditions, topographic highs roughly center around stations 9.8 and 3.3 m, each displaced a short distance downstream from the locally widest points at stations 10 and 3.5 m, respectively. For all six SS conditions, a topographic low roughly centers around station 8 m, also displaced a short distance downstream from the locally narrowest point at station 8.15 m. An additional topographic low emerges at station 15 m for the 80 L/s SS. Roughened channel segments occur elsewhere, which we define by local bed topographies with variations that scale as a few multiples of

Table 2
Values of Downstream Width Change Between Subsampling Locations

	Bounding subsampling locations										
	2,000	3,000	4,000	5,000	6,000	7,000	8,000	9,000	10,000	11,000	12,000
Downstream	to	to	to	to	to	to	to	to	to	to	to
Width Change	3,000	4,000	5,000	6,000	7,000	8,000	9,000	10,000	11,000	12,000	13,000
$\Delta w(x)$	−0.113	0.187	−0.056	0.005	0.089	0.059	−0.252	−0.107	0.178	−0.065	0.072

Note. Downstream width change calculated for length scale $\Delta x = 1.0$ m. Downstream width change calculated as a backward difference with origin at the downstream end (numerator operation reverse of equation (10) or (6)). A backward difference was used for downstream width change in order to assign a negative difference for channel narrowing, and vice versa for widening.

the bed surface D_{90}, and visually appear as a randomly sorted coarse bed surface. The 42 L/s supply conditions had SS conditions with high relative bed elevations compared to the 60 and 80 L/s SS conditions (Figure 7).

We show the SS topographic conditions in more detail with longitudinal profiles (Figure 8). Pools, riffles, and roughened channel segments are qualitatively identified with the zero-crossing (Melton, 1962; Richards, 1976a) and residual depth methods (e.g., Zimmermann et al., 2008b) for minimum continuous length scales of $\bar{w}$. We distinguish pools in two ways. First, as negative residual departures from the detrended profile and, second, as residual depths that occur above the detrended profile but lie below a downstream controlling elevation (i.e., backwater zones). We identify riffles as positive residual departures, and roughened channel segments have minor residual departures that fluctuate around the detrended profile. Figures 7 and 8 illustrate that pools colocate with points of narrowing, riffles with points of widening, and roughened channel segments where width changes are relatively minor.

The physical character of pools at SS strengthens with increasing flow and sediment supply rates. As flow increases from 42 up to 80 L/s and sediment supply from 0.5 to 1.0 kg/min, pool depth and spatial extent generally increase (Figure 8). The SS profiles also reveal that topographic relief increases with flow and sediment supply rates but that channel-averaged longitudinal bed slopes decrease. PRE1 began from an initial slope of 0.015, steepens to 0.0191 at $t_e = 2{,}150$ min, decreases to 0.0162 at 2,390 min, and decreases yet more so to 0.0138 at 2,630 min. We observe a similar progression of bed slope steepening and shallowing for the repeat phase: 0.0186 at $t_e = 4{,}310$ min, 0.0156 at 4,550 min, and 0.0141 at 4,790 min.

The overall organization of average bed elevation in relation to channel width for the six SS conditions is shown in Figure 9. We normalize average bed elevation and channel width by the respective flume-wide means, $(\eta/\bar{\eta})$ and $(w/\bar{w})$, with $\bar{\eta}$ calculated for each SS. The range of bed elevations, given by the box ends, for any value of $w/\bar{w}$ is large for smaller values of the mobility condition τ/τ_{ref} and diminishes with increasing values from 42 to 60 L/s (Table 1 and Figure 9). There is not much, if any differences of relative elevation ranges between 60 and 80 L/s. On the other hand, topographic relief is relatively large for increasing values of τ/τ_{ref} and diminishes with decreasing mobility conditions (Table 1). This result is reflected by the range of $\eta/\bar{\eta}$ values shown in the box plots (Figure 9), and by the departure of the distribution of $\eta/\bar{\eta}$ values from the 1:1 line, which diminishes for increasing values of τ/τ_{ref}. Normalized average bed elevation responses are similar between the initial and the repeat experimental phases. Last, the distribution of normalized elevations highlights three classes of topographic response. Topographic lows relative to the flume-wide average elevation occur at relatively narrow locations ($w/\bar{w} \lesssim 0.80$). We call this the "entrainment response" (Figure 9). Topographic highs occur at relatively wide locations, which we term the "depositional response" ($w/\bar{w} \gtrsim 1.20$). Topography of relative low spatial variation occurs at locations where ($0.80 \gtrsim w/\bar{w} \gtrsim 1.20$). At these locations box and whiskers generally fall around an elevation ratio value of one, and we refer to this as the "intermediate response."

Finally, the spatial organization of average bed elevation in relation to channel width is shown for SS at $t_e = 2{,}150$ and 2,630 min in Figure 10. Axes are the same as those of Figure 9. The two SS profiles indicate that similar values of $w/\bar{w}$ generated differing topographic responses relative to the SS flume-wide average elevation. The magnitude of dissimilarity between topographic differences for any given value of $w/\bar{w}$ depended on the mobility condition τ/τ_{ref}. Lower relative mobilities correlate with more accentuated differences (Table 1), and higher mobilities less differences. The lines and station call outs shown along topographic trace segments correspond to specific pool, riffle, and roughened channel structures within the experimental channel

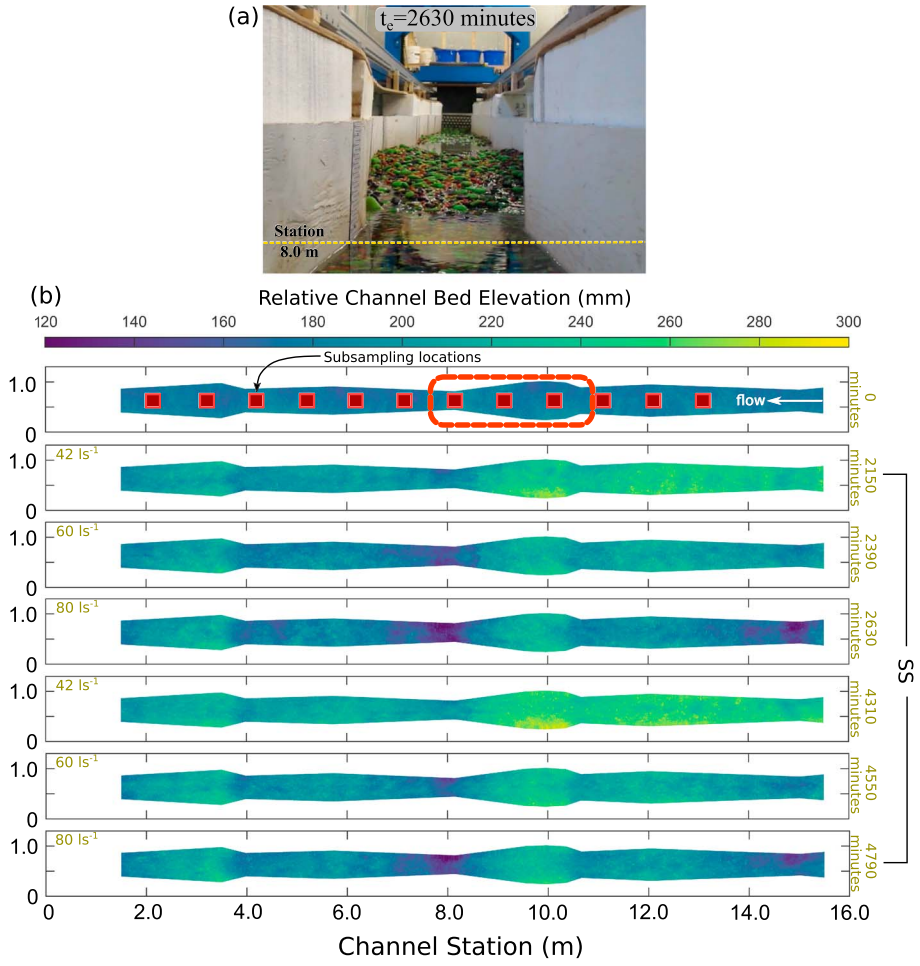

Figure 7. Photograph of experimental conditions for PRE1 and summary panel of topographic responses observed at t_e = 0 min and steady state conditions. Panel (a) shows experimental bed conditions for t_e = 2,630 min looking upstream from station 7.8 m. All other photograph details same as those for Figure 6a. Panel (b) shows topographic responses for the six PRE1 steady state conditions at t_e = 2,150; 2,390; 2,630; 4,310; 4,550; and 4,790 min (Table 1). At the side of each DEM we provide the elapsed time, and within each DEM we indicate the flow rate for the preceding experimental interval. It is of note that Repetto et al. (2002) provide a photograph that shows similar topographic responses to those displayed in (a). See Figure 13 therein.

(Figure 8). Comparison of Figures 7 and 10 reveals that bed topography is organized by downstream width change sequences expressed by riffle-pool (e.g., station 9.96 to 8.14 m: widening to narrowing), or pool-riffle (e.g. station 3.99 to 3.50 m: narrowing to widening) bed morphology.

4.4. Summary of Main Results

PRE1 produced pool-riffle and roughened channel structures that persisted as average mobility conditions $\tau/\tau_{ref} \rightarrow 2$. Pools colocate with points of width narrowing, where $w/\bar{w} \lesssim 0.80$, riffles with points of widening, where $w/\bar{w} \gtrsim 1.20$, and roughened channel beds occur along segments where width change is constrained to the range $0.80 \gtrsim \bar{w} \lesssim 1.20$. The topographic and sediment texture of pools, riffles, and roughened channel beds develop rapidly during the activation time t_a and evolve more slowly thereafter as conditions tend to steady state. The timescale of topographic and sediment texture adjustment from one steady state to another generally varies with the upstream water and sediment supply magnitudes. The combined results suggest that bed topography, and to a lesser degree bed surface texture, are coupled to downstream changes to channel width. This finding provides a link with equation (11), and the control parameter Λ.

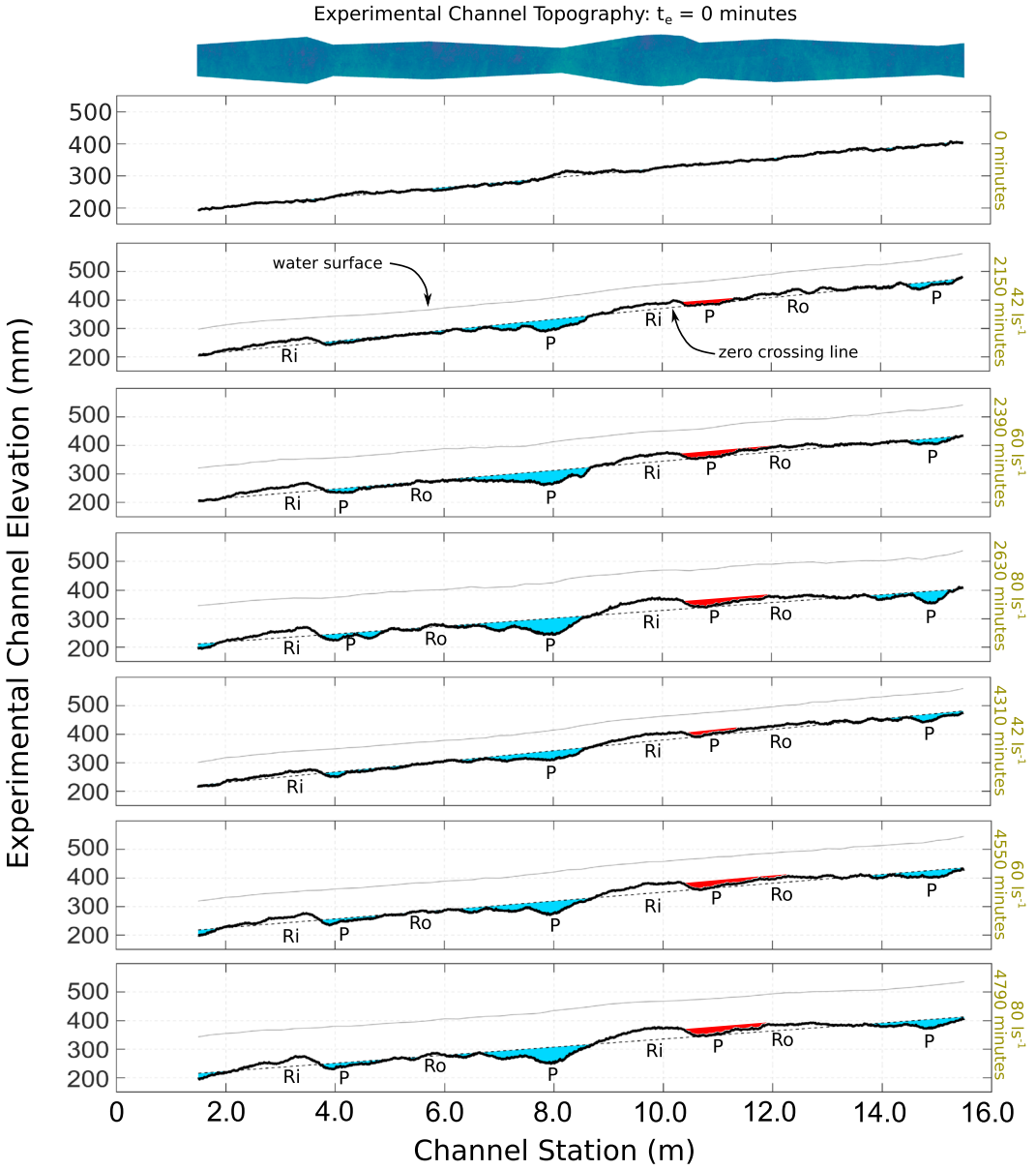

Figure 8. Identification of pool-riffle structures with the zero-crossing and residual depth methods for PRE1 steady state (SS) conditions. DEM of channel at t_e = 0 min shown at top for reference. Zero-crossing profiles (Richards, 1976a) projected onto the experimental channel slope for the six PRE1 SS conditions. Profiles are computed for the center 100 mm of each corresponding DEM. We indicate the general topographic response for each SS case with the abbreviations P (pool), Ri (riffle), and Ro (roughened channel). Pools of light blue fill identified with the zero-crossing method. Pools of red fill identified with the residual depth method. The t_e and Q_w for the preceding experimental interval are given to the right of each profile. The water surface profile is represented by the light solid line, and the zero-crossing line is represented by the light dashed line, specifically called out for t_e = 2,150 min. The water surface profile is smoothed from the measured profile with a forward and backward moving average of 1–3 nodes in length. The number of nodes is chosen by minimizing the root-mean-square error between the smoothed and measured profiles.

5. A Mechanical Link Between Channel Width Variations and the Gravel Bed Topographic Response: Theory Evaluation

In section 2 we introduce a scaling-based model for S_{local}. The model predicts that S_{local} is a function of the parameter Λ, and the downstream variation of the dimensionless streamwise velocity. Here we make direct connections between equation (11) and PRE1, with an emphasis on those aspects of observed conditions which relate to Λ.

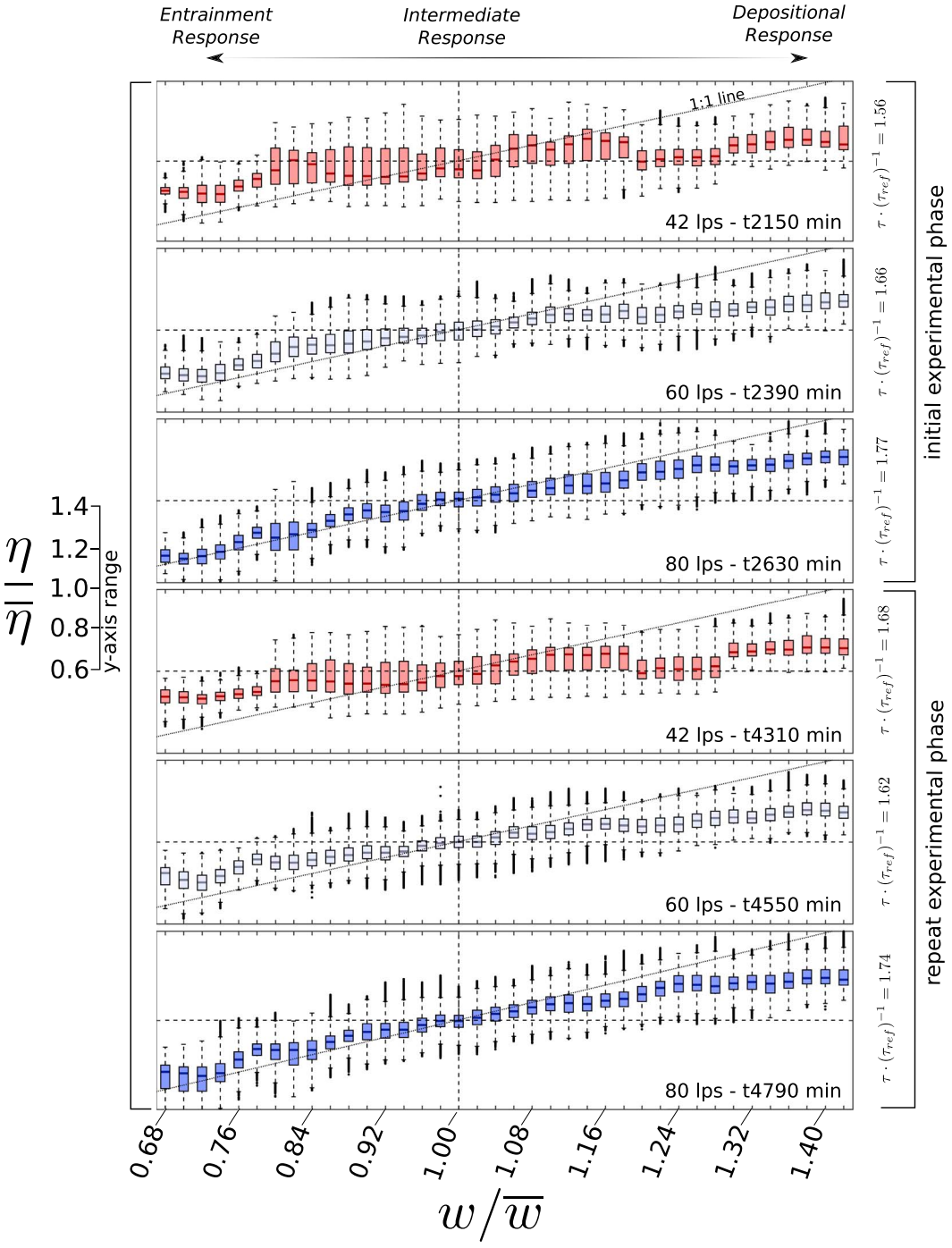

Figure 9. Summary panel of PRE1 steady state topographic responses illustrated with box-and-whiskers plots. The physical nature of responses is provided at the top of the panel, and mobility condition τ/τ_{ref} is provided to the right. The term w is the local channel width; $\bar{w}$ = 547 mm and is the mean channel width of the experimental channel, η is the local elevation provided by the DEM, and $\bar{\eta}$ is the mean elevation of the experimental channel for each steady state condition. The y axis range is consistent for all six subplots. Box colors indicate flow magnitude. Values have been binned into 0.02 bin classes of $w/\bar{w}$.

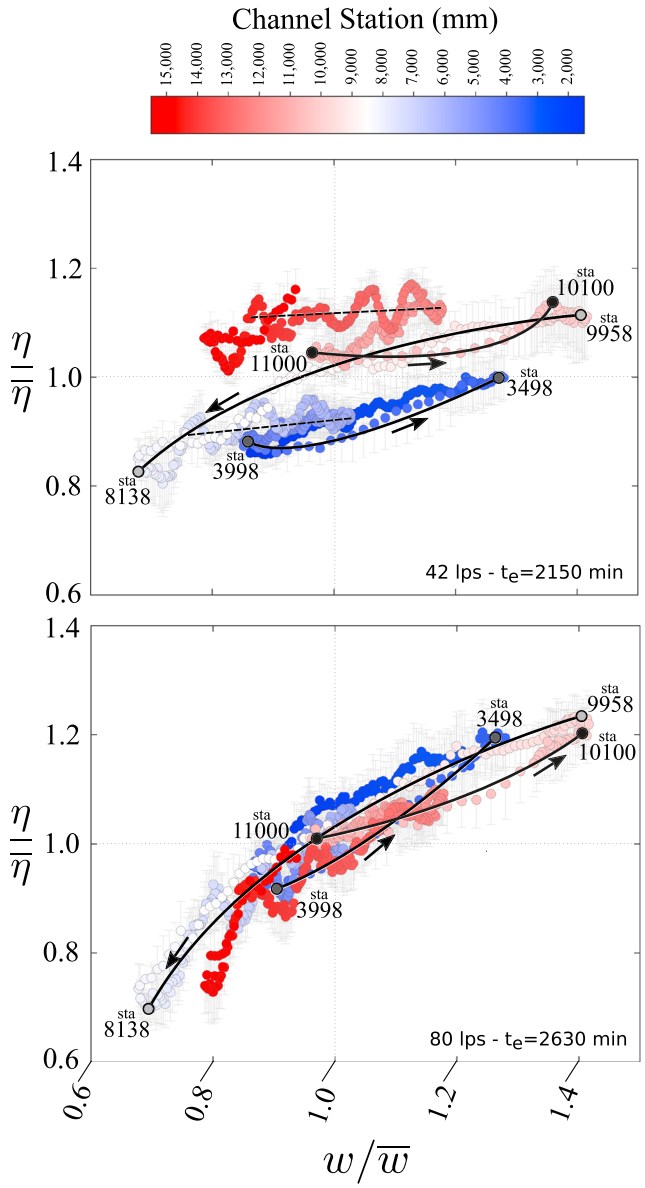

Figure 10. Profile traces of topographic response for steady state conditions at $t_=$ 2,150 and 2,630 min. Same axes as used in Figure 9. Color bar denotes location along experimental channel (see Figure 6). The individual elevation points (circles) along the profile traces reflect the median values shown in the box plots from Figure 9, and the error bars correspond to the whisker range. The arrows indicate the downstream direction along the profile traces and in between station callouts.

5.1. Downstream Changes of Flow Velocity, Particle Mobility, and Λ

How does channel narrowing and widening ultimately lead to pools and riffles? We expect from Λ and volume conservation $Q = \bar{U}_x A$ that the cross-sectionally averaged shear velocity and flow velocity, respectively, and hence particle mobility, will increase for channel narrowing and decrease for widening. This expectation is generally demonstrated in Figure 11 for the 12 subsampling locations shown in Figure 2. At each subsampling location, volume conservation is used to solve for the spatially averaged cross-sectional flow velocity $\bar{U}_x = (Q/A)$. In order to remain consistent with the shear velocity calculation discussed in section 2, particle mobility was calculated according to the Shields equation (Shields, 1936): $\tau^* = \tau/(\rho_s - \rho_w g D_{50})$. As noted in section 2, using the depth-slope product under the uniform flow approximation does introduce uncertainty, but it does not affect the spatial trends because flow depth and water surface slope are spatially correlated with channel width (see supporting information S2 for relevant plots). To confirm this, particle mobility was calculated with

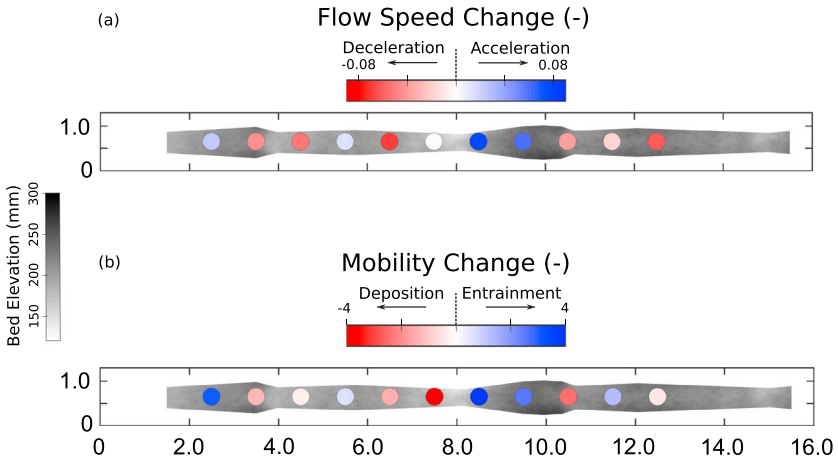

Figure 11. Average steady state topography related to downstream changes in (a) normalized cross-sectionally averaged flow velocity: $U_x/\bar{U}_x$, and (b) normalized sediment mobility: $\tau^*/\tau^*_{\text{ref}}$. Average topography determined from the PRE1 SS conditions (Table 1). Change in downstream flow velocity and mobility determined as backward differences for all subsampling locations, with the origin at the downstream end and averaged across observational times 1–29 (Table 1). Changes are plotted midway between subsampling locations. Flow velocity normalized by the mean flow velocity for all subsampling locations and PRE1 observation times, and mobility normalized by a $\tau^*_{c_{50}} = 0.035$.

a drag type stress relation and with the Manning-Strickler formulation of the Shields equation (Parker, 2007, 2008). In all cases, spatial trends were consistent between the different calculation procedures. One PRE1 value of $S < 0$ used in the Shields equation was set to $S = 0.005$. Setting S to a smaller value accentuates predictions more strongly and does not change spatial trends.

Figure 11a shows that, in general, flow velocity declines in segments of channel widening (warmer colors), increases along segments of narrowing (colder colors), and has negligible variation in straight segments where downstream width changes are small (neutral colors). The spatial pattern of flow velocity change for widening and narrowing segments is consistent with results and explanations provided through field-based studies (Furbish et al., 1998; Hassan & Woodsmith, 2004; MacVicar & Roy, 2007a; Thompson et al., 1999), numerical simulations (de Almeida & Rodríguez, 2011; MacWilliams et al., 2006), and theoretical efforts coupled with experimentation (Repetto et al., 2002). The spatial pattern of flow velocity change correlates with the spatial pattern of SS bed topography suggesting a mechanistic link. In general, pools occur where flows accelerate, reflecting net particle entrainment, riffles where flows decelerate, reflecting net particle deposition, and roughened channel segments where flow velocity change is negligible (Figure 11a; cf. Figure 8). However, pools at stations 4 and 10.6 m depart from the general velocity-topography spatial correlation. This suggests that there is an alternative explanation which explains how these structures form.

Figure 11b shows that, in general, particle mobility declines in segments of channel widening (warmer colors), increases along segments of narrowing (colder colors), and has negligible variation in straight segments where downstream width change is minor (neutral colors). However, as with velocity, there are departure from these general spatial correlations. Station 7.5 m shows relatively low topography, but a strong depositional prediction (bright red circle), and station 4.5 m is topographic relative low, and also shows a weaker depositional prediction (light red color). The primary factor driving this discrepancy at both locations is a relatively large decrease in the water surface slope. Figure 11a also shows that flow velocity changes very little from station 8.5 to 7.5 m, thus favoring particle entrainment conditions, as captured by the DEM. The relationship between spatial patterns of flow velocity change, particle mobility and SS bed topography is consistent with field measurements of riffles located at points of widening, where flow decelerates, and pools located at points narrowing, where flow accelerates, within alluvial (MacVicar & Roy, 2007a) and bedrock river reaches (Venditti et al., 2014). Furthermore, the coupling of downstream changes to channel width, flow velocity

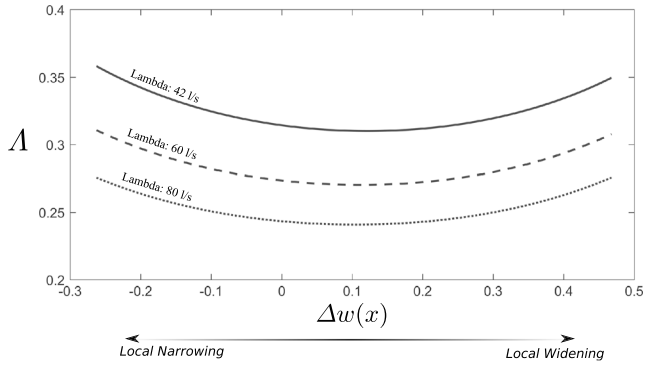

Figure 12. Plot of Λ of equations (11) and (12) across the width change parameter space for PRE1 steady state conditions at 42, 60, and 80 L/s. Shear velocity calculated as the depth-slope product (see section 2).

change, particle mobility, and bed topography shown in Figure 11 is consistent with theory and field measurements (Furbish, 1998; Furbish et al., 1998) and is in general agreement with the flow convergence routing hypothesis of MacWilliams et al. (2006).

Figure 12 shows that Λ has a parabolic-like shape for the 42, 60, and 80 L/s steady state conditions. Maximum Λ values occur for the largest width change conditions, and the parabolic-like shape is not symmetrical about $\Delta w(x) = 0.0$ but does show rough symmetry about $\Delta w(x) = 0.1$. The parabolic-like shape of Λ suggests that w and u_* are coupled in a complementary manner as downstream width changes from narrow to wide, and vice versa. Evidence of a complementary relationship between w and u_* is provided within Figure 13, which shows that u_* varies inversely with w. This result supports our interpretation of Λ discussed in section 2 (see equations (13) and (7) and associated discussion). Furthermore, Figure 12 and the dependence of u_* on τ indicates that our results are consistent with previous numerical and field-based studies, which show a spatial organization of u_* and τ between pool and riffle, with higher values located within pools and pool tail outs, and lower values over the head of riffles (Carling, 1991; Carling & Wood, 1994; MacWilliams et al., 2006; MacVicar & Roy, 2007a; Thompson & Fixler, 2017; also see discussion of ; Keller, 1969, in ; MacWilliams et al., 2006). Λ has a minimum for $\Delta w(x) = O(0.1)$. This result indicates that differences between t_f and t_y are maximized around $\Delta w(x) = O(0.1)$ for PRE1 conditions. Additional testing with numerical and field data sets is needed to determine if this particular relationship between t_f and t_y around $\Delta w(x) = O(0.1)$ is a general condition of gravel bed mountain streams, or whether it is specific to the PRE1 experimental conditions.

5.2. Downstream Changes of Local Channel Width and Bed Slope

Figure 14 illustrates the average local channel bed slope $\bar{S}_{\text{local}}$ versus the associated downstream change in width $\Delta w(x)$ for PRE1 SS conditions, building from the general recognition of a link between channel width and bed slope by MacVicar and Roy (2007a, Figure 1 therein). Here downstream width changes $\Delta w(x)$ and corresponding local bed slopes $\bar{S}_{\text{local}}$ were evaluated in between points of major inflection in the width profile. This was done in order to incorporate data from the literature, and do so in an analytically consistent manner (see supporting information S3). Local channel widths and bed elevations used to compute $\Delta w(x)$ and $\bar{S}_{\text{local}}$ represent spatial averages over subsampling locations centered around the width inflection points. Subsampling regions measured 180-mm upstream and downstream of inflections for channel width, and $320 \cdot 320$ mm^2 for local bed slope (see supporting information S1 and Figure 2).

Figure 14 highlights three important points. First, as channel segments increasingly narrow, local bed slope steepens in the downstream direction (positive values of $\bar{S}_{\text{local}}$). Second, as channel segments increasingly widen, slopes decline and can be adverse (negative values of $\bar{S}_{\text{local}}$). Third, segments which exhibit little change in width have comparatively smaller local bed slopes (positive and negative, depending on the sign of the width change) versus conditions where the local width change is stronger. In a downstream-moving reference frame, PRE1 data plotted in Figure 14 suggest that pool-type structures are favored where reductions of channel width are relatively large, the bulk flow is accelerating, and $\tau^* \gg \tau^*_{\text{ref}}$. On the other hand, riffle-type deposits are more likely where increases of channel width are relatively large, the bulk flow is decelerating, and $\tau^* \ll \tau^*_{\text{ref}}$. Last, roughened channel beds occur for negligible changes in width, positive or negative, for which the downstream bulk flow velocity change is minor, and $\tau^* \approx \tau^*_{\text{ref}}$ (Table 3 and Figure 11). In the context of Λ, pool- and riffle-type structures are most likely to occur for increasing values of Λ, and roughened channel beds where Λ is approaching a minimum (cf. Figures 12 and 14).

PRE1 experimental data are supplemented in Figure 15 with corresponding data calculated for experimental results reported by Nelson et al. (2015), field-based results reported by Thompson et al. (1999), and numerical simulation results reported by de Almeida and Rodríguez (2012) and Bolla Pittaluga et al. (2014; see supporting information S3 for details of how $\Delta w(x)$ and S_{local} were calculated for each study). Nelson et al. (2015) provide experiments guided by the physical characteristics of the middle reach of the Elwha River, WA, USA; Thompson et al. (1999) provide field data for North Saint Vrain Creek, Rocky Mountain National Park, Colorado;

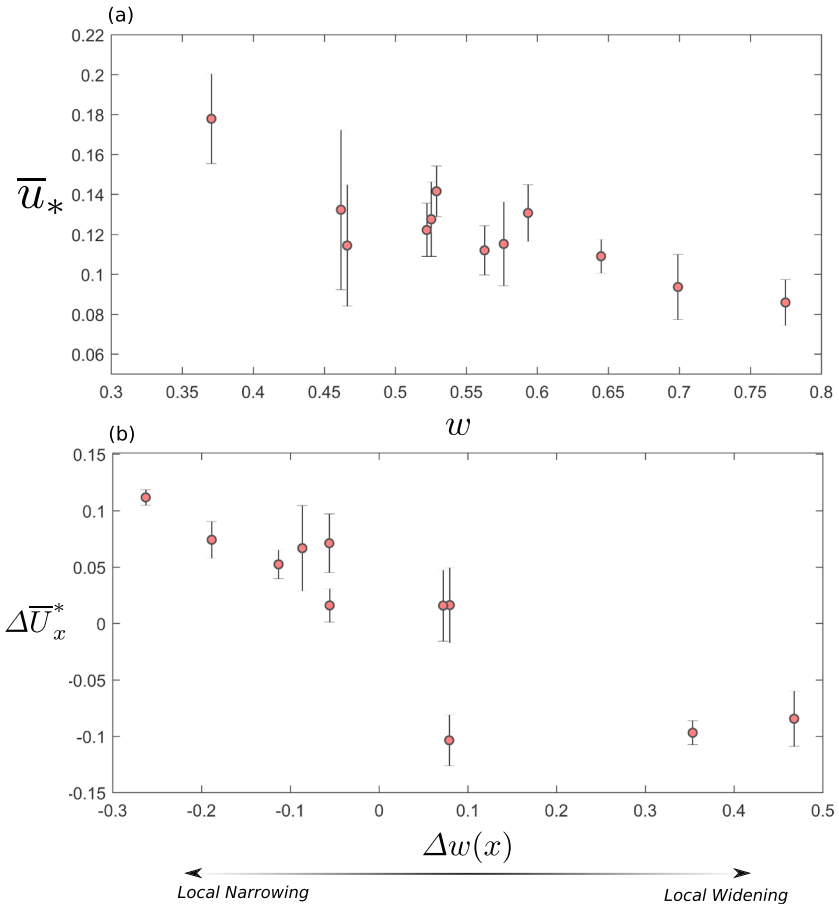

Figure 13. Plot of u_* of equation (12) and ΔU_x^* of equation (11). (a) u_* is plotted as a function of local channel width to be consistent with equation (13) and is calculated as the depth-slope product (see section 2). (b) ΔU_x^* is plotted as a function of the downstream change of channel width. Both quantities are averages for the PRE1 steady state conditions, and the error bars are the standard deviation.

de Almeida and Rodríguez (2012) provide numerical simulations of the Bear River, AK, USA; and Bolla Pittaluga et al. (2014) provide numerical simulations of the Magra River, Italy, used to test theory for the equilibrium profile of riverbeds. Plotted data for de Almeida and Rodríguez (2012), Bolla Pittaluga et al. (2014), and Nelson et al. (2015) are reported as steady state or equilibrium profile conditions. To our knowledge, Thompson et al. (1999) do not report an assumed profile condition.

Figure 15 illustrates that local bed slopes for all sources exhibit a systematic organization across the full range of downstream width change, from (−0.30) to (+0.50). This result is particularly important because reach-averaged bed slopes of the literature-based data sets cover a wide range: 0.0001 (Bolla Pittaluga et al., 2014), 0.002 (de Almeida & Rodríguez, 2011, 2012), 0.0069 (Thompson et al., 1999), and 0.007. These bed slopes stand in contrast to the range of our SS experimental channel bed slopes: 0.014 to 0.019. This difference highlights consistency between bed slope response and width change across almost two orders of magnitude of reach-averaged bed slope.

Figure 15 shows two different predictions of S_{local} calculated with equation (11) (see supporting information S2 for details of calculation procedure). The two predictions correspond reasonably well except at the extremes, and both predictions reproduce the general data trend well, despite the simplifying assumptions underpinning derivation of equation (11). The gray shaded region was calculated using the depth-slope formulation of the shear velocity, with the full range of local SS water depths and water surface slopes measured during PRE1 (see section 2). The dashed line was calculated using the Manning-Strickler formulation of the shear velocity (see figure caption for details). The two contrasting calculation procedures offer one sensitivity test to the manner in which S_{local} is modeled with equation (11).

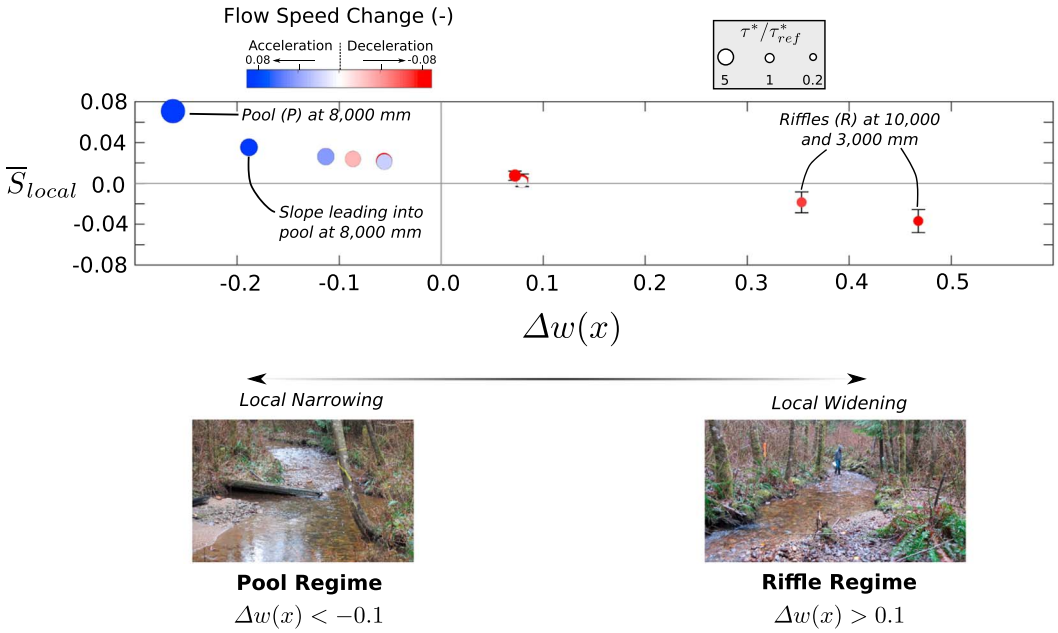

Figure 14. Average channel bed slope as a function of the downstream change to channel width, flow velocity, and particle mobility. Local bed slope is calculated as the forward difference between major inflection points of channel width (see Figure 2) with the origin at the downstream end, averaged for the PRE1 steady state conditions (Table 1). Error bars represent the sample standard deviation. Flow velocity change is depicted by color, and the $\tau^*/\tau^*_{\text{ref}}$ magnitude is indicated by circle size. Pool and riffle labeled points correlate most clearly with the mechanical coupling between width, flow velocity, and particle mobility change moving downstream.

The depth-slope-based prediction matches the trend of plotted data better for relatively large positive width gradients due to the effect of diminishing water depths and flattening water surface slopes on the calculated shear velocity at riffles. This affect is not captured by the Manning-Strickler formulation. The predictions track in a relatively tight fashion across intermediate negative and positive values of $\Delta w(x)$ and begin to diverge slightly as channel narrowing tends to a value of −0.30. Differences grow as the narrowing condition strengthens because shear velocities with the depth-slope formulation increase faster than with the Manning-Strickler formulation. This is due to the relatively high water surface slopes measured at the pool for station 8 m (cf. Figure 8), relative to the reach average value used for the Manning-Strickler-based calculation. Despite these differences, the key is recognition of a coupling between local width organization, flow velocity, bed surface particle mobility, and bed topography. The details of how this information is used to approximate the forces imparted to the bed surface serve to refine or generalize the prediction, and for the two approaches tested, do not change the ultimate interpretation of this coupling.

Table 3
Mean Values of $U_x/\bar{U}_x$ and τ^*/τ^*_{ref} for Subsampling Locations

	Subsampling locations										
	3,000	4,000	5,000	6,000	7,000	8,000	9,000	10,000	11,000	12,000	13,000
Normalized Velocity											
$U_x/\bar{U}_x$	0.939	0.980	0.990	1.010	1.056	1.064	0.979	0.951	1.004	0.988	1.040
Normalized Shields Stress											
$\tau^*/(\tau^*_{\text{ref}})$	0.150	1.674	0.962	0.321	0.546	3.892	1.120	0.367	1.315	0.476	0.990

Note. U_x is averaged across all times. $\bar{U}_x$ is the average for all subsampling locations for all times. The τ^* is averaged across all times.

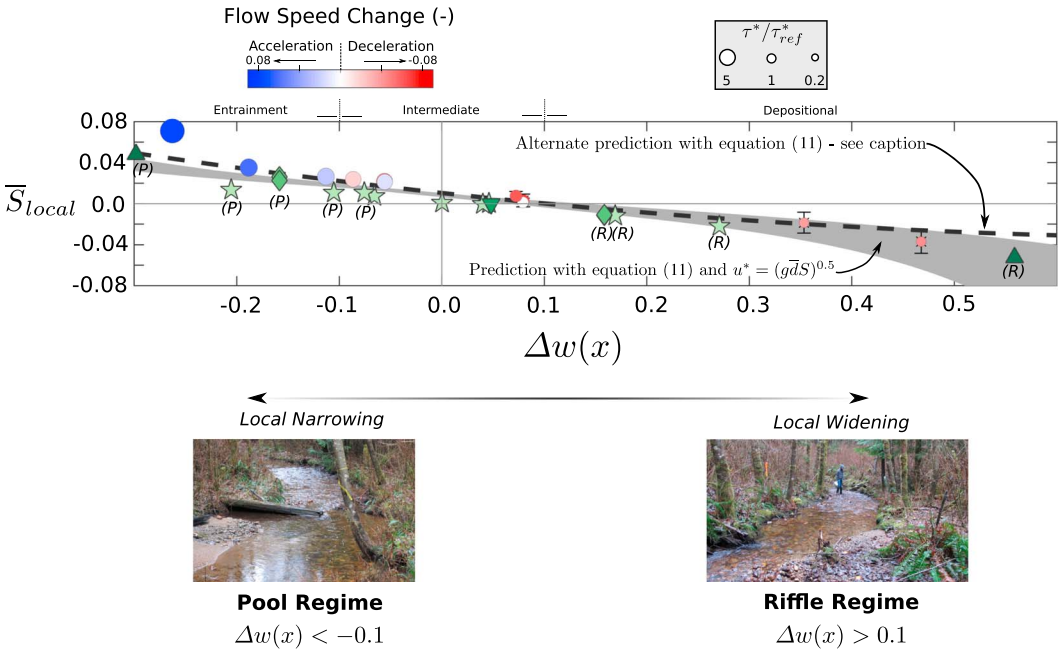

Figure 15. Average channel bed slope as a function of the downstream change to channel width, flow velocity, and particle mobility for PRE1 with additional data and theory evaluation. To the data plotted in Figure 14, we add data calculated from Thompson et al. (1999; right-side up triangles: data from Figure 2 therein), de Almeida and Rodríguez (2012; stars: Figure 2 therein), Bolla Pittaluga et al. (2014; upside down triangle: data from Figure 7 therein), and Nelson et al. (2015; diamonds: mean of data from Run 1 in Figure 6 therein). For literature-based data sources we use *P* to indicate pool and *R* for riffles, based on the authors' assertions or our own visual interpretation of the profiles. The alternate prediction with equation (11) was calculated with the Manning-Strickler form of the shear velocity: $u_* = \left(\left[k_s^{0.33} q_w^2 / (\alpha_r^2) \right]^{0.30} [gS]^{0.70} \right)^{0.5}$ (e.g., Parker, 2008), where S was set to the steady state flume-wide average channel bed surface slope ≈ 0.015. See supporting information S3 for details of how $\Delta w(x)$ and S_{local} were calculated for each data source. Size of the symbols used for external data sources provides for roughly 10% uncertainty in calculations.

6. Discussion

The combined results of sections 2, 4, and 5 raise several points which require discussion. First, Figure 14 illustrates basic agreement between the proposed mathematical model of S_{local} and organization of local topographic gradients across the parameter space of downstream width change $-0.3 : +0.5$. How can this result be synthesized with respect to pool-riffle formation, or more generally, pool-riffle occurrence? Second, Figure 8 illustrates that spatial patterns of S_{local} are similar across a range of water and sediment supply conditions that vary by a factor 2. In particular, what does persistence of pool, riffle, and roughened channel bed structures at the largest flow and sediment supply rates suggest for pool-riffle persistence? Third, results presented in Figures 7 and 8 suggest that pool-riffles are created by at least two different processes along variable width channels. What are these processes?

6.1. Synthesis of the Coupling Between Local Width Variations and Bed Slope

Figure 14 demonstrates a mechanical link between downstream variations of local channel width and bed slope that is generally consistent with our proposed scaling-based theory. This finding is supported by five different data sets that include experimental work (PRE1 reported here and in; Nelson et al., 2015), field data (Thompson et al., 1999), and numerical simulations (Bolla Pittaluga et al., 2014; de Almeida & Rodríguez, 2012). Overall congruence between and among these data sets, and with the theory of equation (11), is important for three reasons. First, we derive equation (11) assuming steady state conditions, and we calculate u_* with the uniform flow approximation. Natural flows in rivers are seldom uniform (e.g., Paola & Mohrig, 1996), and neither were the PRE1 experimental flows. Second, MacWilliams et al. (2006) present discussion and results that outline the difficulty of estimating τ, and consequently u_*, with one-dimensional representations of the water surface slope. This problem is less severe for PRE1 because channel width variations are symmetrical about the center streamwise coordinate (Figure 2), and bed topography was approximately uniform in the cross-stream direction (cf. Figure 7). But river segments with significant cross-stream flow patterns are less

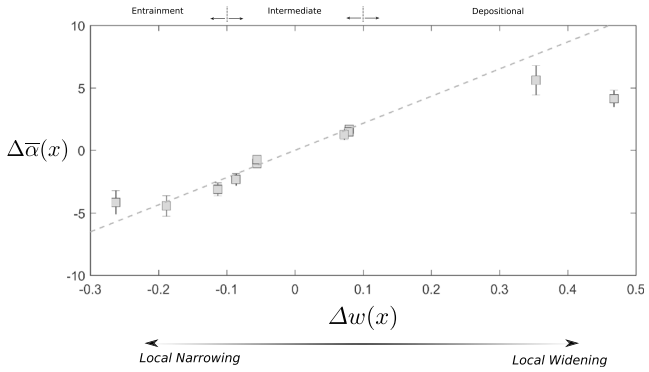

Figure 16. Average width to depth ratio difference $\Delta\tilde{\alpha}$ as a function of the downstream change to channel width. $\Delta\tilde{\alpha}(x)$ calculated as a forward difference between subsampling locations (see Figure 2) with the origin at the downstream end, averaged across the PRE1 steady state conditions. The error bars are the standard deviation. The light gray dashed line is a linear best fit to $\Delta\tilde{\alpha}(x)$ with a coefficient value of 22, as we know of no theory to predict $\Delta\tilde{\alpha}(x)$.

amenable to one-dimensional approximations (see discussion in; MacWilliams et al., 2006). Third, the PRE1 setup was defined by channel bank walls that contained all experimental flows. Therefore, width variation was the dominant local driving mechanism of bed topography. Alluvial rivers which express pool-riffle bed architecture, however, rarely contain flood flows up to the approximate 5-year flood, let alone a 10-year flood, except perhaps over relatively short lengths. Therefore, experimental containment of all PRE1 flows represents a clear limitation of our work and introduces uncertainty in directly applying our findings to natural pool-riffles formed within floodplain environments. Furthermore, PRE1 flow containment accentuates the experimental affect of downstream channel width variation on local bed profile development and evolution, as compared to natural pool-riffle stream segments which commonly form and evolve within the context of overbank flows during relatively large floods. Despite these challenges and limitations, we capture the basic width variation dynamic mathematically with $\bar{U}_x^*$ and Λ of equations (8) and (13), respectively. Through this we learn that $\Delta w(x)$, $\bar{U}_x$, and u_* are coupled in an overall predictable manner (e.g., Figure 11a and inset plot of Figure 12). We therefore propose that the primary link connecting experimentation, numerical simulation, and nature is a spatial variation of channel geometry that causes flow to locally change speed. Changes of flow speed influence patterns of sediment entrainment and deposition (e.g., Ancey, 2010; Exner, 1925; Paola & Voller, 2005) that scale in length as $\approx \bar{w}$ (e.g., Clifford, 1993; MacWilliams et al., 2006). We expand this discussion below.

Motivated by the findings of Figure 14, we tentatively identify three dynamical regimes in terms of the $\Delta w(x)-S_{\text{local}}$ parameter space, which express thresholds for the occurrence of pools and riffles:

$$\text{Slope Regimes}=\begin{cases}\text{Entrainment Regime:} & \Delta w(x) < -0.1 \text{ and } S_{\text{local}} > 0.2\\ \text{Intermediate Regime:} & -0.1 < \Delta w(x) < 0.1\\ & 0.02 > S_{\text{local}} > -0.1\\ \text{Depositional Regime:} & \Delta w(x) > 0.1 \text{ and } S_{\text{local}} < -0.1\end{cases}$$

Pool development defines the entrainment regime, driven by the downstream flow which is accelerating, $\tau^*/\tau^*_{\text{ref}}$ values, which are well above threshold conditions and Λ values, which are increasing. Roughened channel development defines the intermediate regime, driven by the downstream flow, which is approximately uniform for $\Delta x \approx 1-3\bar{w}$, mobility conditions that are near the threshold condition, and Λ values that are converging to a minimum. Riffle construction defines the depositional regime, driven by the downstream flow which is decelerating, mobility conditions that are well below the threshold condition (cf. Table 3), and Λ values, which are increasing. Last, it is unknown if combinations of $+\Delta w(x)$, $+S_{\text{local}}$ and $-\Delta w(x)$, $-S_{\text{local}}$ are associated with observable natural river conditions that persist for timescales of longitudinal profile equilibrium (e.g., Blom et al., 2016, 2017; Mackin, 1948). At shorter timescales of flood events, Brown and Pasternack (2017) suggest that $+\Delta w(x)$, $+S_{\text{local}}$ can result along natural rivers due to net local bed erosion of a relatively wide segment during a large flood. Erosion could be driven by a flow obstruction or channel curvature. Similarly, Brown and Pasternack (2017) imply that $-\Delta w(x)$, $-S_{\text{local}}$ can result due to landsliding of relatively immobile granular material into a segment of channel narrowing. Furthermore, results from the authors' field test reveal that these two combinations of local width and slope change are less common along their Yuba River, CA, field site, and less strongly expressed, compared to the reverse cases, which reflect the results of Figure 14.

Equation (11) indicates that local slope construction depends on the magnitude of Λ, and the sign and magnitude of ΔU_x^*. Careful consideration of equation (13) with Figures 12 and 13a reveals that relative changes of u_* are proportional to relative changes of w between pools and riffles of PRE1. For example, absolute values for predicted pool and riffle local bed slopes are comparable (Figure 15). Based on Λ, this outcome can only happen if local width and shear velocity change by approximately consistent factors, noting that ΔU_x^* exhibits a similar range of values greater than, and less than 0 for our linear approximation of the PRE1 ΔU_x^*-$\Delta w(x)$ inverse relationship (Figure 13b and see supporting information S2). This finding is surprising in the context

of Figure 15 for two reasons. First, it implies that the plotted literature-based data sets intrinsically contain a covariance structure between local width and shear velocity that is similar to PRE1 conditions (this assumes that affects related to variation of D_{90f} and ε between data sets is relatively small by comparison—which may not be the case). Although we cannot definitively demonstrate this point at this time, this possibility expands on the covariance proposal of Brown and Pasternack (2017) by providing a mechanistic explanation for the spatial organization of S_{local} along pool-riffle channel segments, which exhibit downstream changes to channel width. Second, the nature of feedbacks between u_* and w for PRE1 are forced by the fixed experimental channel wall positions. This is a simplification of natural rivers for which the feedback goes both ways because channel width evolves through time, and u_* responds to this evolution, and vice versa. Furthermore, morphodynamic feedbacks driven by temporal and spatial variations of D_{90f} and ε may also be important under certain conditions. These last two points are important to recognize because the combination of these influences within natural pool-riffle streams may result in positive feedbacks between t_y and t_f, as compared to the more limited reinforcing feedback discussed in section 2.

In the context of the preceding discussion and Figure 15, it is important to note that plotted values of S_{local} vary for similar values of $\Delta w(x)$, and in relation to the predictions of equation (11). The latter result is expected, whereas the former result could represent the affect of differences among the associated experiments, field conditions and numerical simulation test cases, which offer additional and contributing explanations of S_{local}. For example, width variation is rarely symmetrical along natural streams and is commonly caused by bedrock outcrops (e.g., Lisle, 1986), immobile boulders (e.g., Thompson et al., 1999), or landslide-type deposits, which impinge on the channel margins. The variability of S_{local} could also reflect differences between sediment supply composition and or hydrologic regime, and the general presence or absence of instream large wood (Buffington et al., 2002). Whereas the PRE1 experimental design and conditions support assignment of a cause and effect link between local width variations and bed slope development, the same conclusion cannot be made for the other data sets of Figure 15, in particular the field case of Thompson et al. (1999). Nonetheless, we suggest that the overall evidence presented here supports the general explanation of S_{local} by equation (11) and that local width variations are a critical element of the conditions which lead to pool-riffle formation along natural rivers (e.g., Clifford, 1993; MacWilliams et al., 2006). If other factors prove to be important in explaining S_{local} from a mechanics perspective, we suspect that their overall physical affect will be similar to the points raised and discussed here.

6.2. Width/Depth Ratio Change as a Metric of Morphodynamics

Figure 16 illustrates that downstream changes to the local average width to depth ratio $\Delta\tilde{\alpha}(x)$ vary linearly with $\Delta w(x)$. To help understand what this means, we identify three $\Delta w(x)$-$\Delta\tilde{\alpha}(x)$ regimes:

$$\text{Width/Depth Regimes}=\begin{cases}\text{Depth Regime:} & \Delta w(x) < -0.1 \text{ and } \alpha < -2\\ \text{Intermediate Regime:} & -0.1 < \Delta w(x) < 0.1 \\ & 2 > \alpha > -2\\ \text{Width Regime:} & \Delta w(x) > 0.1 \text{ and } \alpha > 2\end{cases}$$

The depth regime is characterized by water depths that are increasing relative to channel width. As a result, flows are comparatively deep and increasing in speed, delivering more momentum flux to the bed, and it is for such conditions that pools develop. The intermediate regime is characterized by comparable changes in width and depth. As a result, flows are approximately uniform, and it is for such conditions that roughened channel segments develop. The width regime is characterized by channel widths that are increasing relative to water depth. As a result, flows are comparatively shallow and decreasing in speed, and it is for such conditions that riffles develop. Brown and Pasternack (2017) offer a similar type of framework in developing their geomorphic covariance structure proposal.

Within the context of these three regimes, we derive a simple scaling which describes the relaxation length of PRE1 flows to downstream changes of channel width. The linear correlation between $\Delta\tilde{\alpha}(x)$ and $\Delta w(x)$ permits

$$\Delta\tilde{\alpha}(x) \propto \Delta w(x) \tag{15}$$

Because of a coupling between the flow and the bed, $\Delta\tilde{\alpha}(x)$ is a summary of the morphodynamic processes that led to net adjustment of bed topography across the range of imposed width changes. Net adjustment of

bed topography to external conditions is known to converge toward states for which the local divergence of bedload flux goes to zero (equation (1); Bolla Pittaluga et al., 2014). It follows then that $\Delta\bar{\alpha}(x)$ reflects the tendency to balance local flow momentum and resulting solid fluxes. The balancing occurs over a characteristic length scale reflected in the $\Delta\alpha(x)$-$\Delta w(x)$ proportionality, which upon simplification yields

$$\Delta x \approx \chi \Delta\bar{d}, \tag{16}$$

where χ is a scaling factor, which for PRE1 has an approximate value of 22, and $\Delta\bar{d}$ is the downstream change of the cross-sectionally averaged flow depth. For the pool at station 8 m, $\Delta\bar{d}$ has an average approximate value of 40 mm across observations 1–29, whereas for the riffles at stations 4 and 10 m, the average values are −25 and −16 mm, respectively. According to equation (16), this suggests that the specified channel narrowing at 8 m drives a mean flow response which manifests over a relaxation length scale Δx that is roughly twice as long compared to that for the riffles at 4 and 10 m (using the absolute values of $\Delta\bar{d}$ values given). Recalling that $\bar{w}$ for PRE1 was 547 mm, the pool relaxation length at 8 m scales as approximately $2\bar{w}$, and the two riffle relaxation lengths as approximately $\bar{w}$. It is of note that the pool relaxation length scale is similar in magnitude to the flow response length scale reported by MacVicar and Best (2013): $3–4\bar{w}$.

6.3. Natural Development of Bed Topography Along Mountain Streams: Support for an Emerging View

We speculate that the combined results of Figures 7–14 provide preliminary evidence that the combination of PRE1 flows are important for topographic expression, and by extension morphodynamics in natural streams. Experimental support for our proposal consists of two parts. First, pool-riffle and roughened channel persistence across all experimental water and sediment supply conditions suggests that morphologic response is reinforced across the range of supply conditions. Second, increasing topographic relief for lower overall longitudinal gradients, and vice versa, suggests that different supply magnitudes maintain channel form in different, but equally important ways (Figure 8; Bayat et al., 2017).

Our perspective is consistent with the interpretations of Pickup and Rieger (1979), Parker et al. (2003), Bolla Pittaluga et al. (2014), and Brown and Pasternack (2017) that the full distribution of flows under the present day hydrology is important for channel morphology, as raised by Ferrer-Boix et al. (2016). More importantly, however, recognizing the importance of the full hydrologic regime in channel form maintenance builds immediate bridges with ecology, and in particular with the field of environmental flows, and the natural flow paradigm (NFP) concept (e.g., Acreman, Overton, et al., 2014; Poff et al., 1997). The NFP reflects the view that the entire flow regime consisting of droughts, floods of all size, annual low flows, etc., are critical to the support of riverine processes and ecological communities. NFP may seem at odds with the perspective that bankfull, or the effective flood is the most important flow for mountain stream morphologic maintenance (Emmett, 1999; Whiting et al., 1999; Wolman & Miller, 1960). The bankfull or effective flow perspective is based on quantifying the flood magnitude that moves the most bedload sediment over long periods of time. Since alluvial channels are built by sediment transport, it follows that the bankfull or equivalent flow maintains river form or shape. Despite hydroclimatological variation in the frequency of bankfull or effective flows (Williams, 1978), the morphologic basis of bankfull is a critical aspect of geomorphology (Phillips & Jerolmack, 2016).

As a start to bridge the apparent gap between concepts underpinning views of environmental and bankfull flows, we speculate that results presented here coupled with supporting work by Pickup and Rieger (1979), Parker et al. (2003), Bolla Pittaluga et al. (2014), and Brown and Pasternack (2017) highlights that relatively large floods (e.g., 5-year and greater recurrence interval) build the framework, or foundation skeleton of gravel bed mountain streams, and that smaller, more frequent floods fill out the framework, while retaining the shape or morphology of the framework (Figure 8). The filling out process evolves according to the sequence and magnitude of floods, which work collectively to enhance morphologic diversity (Figures 8–10) and build the riverine palette from which measurable ecosystem services are realized (Acreman, Arthington, et al., 2014, Figure 1 therein). Accordingly and over long periods of time, the bankfull or effective flow would be the most important element of the flows which fill out the framework (e.g., Emmett, 1999; Whiting et al., 1999; Wolman & Miller, 1960). However, lower recurrence interval floods are also known to specifically play an important role in pool-riffle maintenance, for which velocity reversal (Keller, 1971) and shear stress convergence (e.g., Rodríguez et al., 2013) between riffle and pool have been shown to have a reinforcing affect on the shape of the local bed profile. Our work and speculation here does not discount the morphologic importance of these lower flows nor does it add to the understanding of how important these lower flows are for pool-riffle morphodynamics.

6.4. Development of Pool-Riffles Along Variable Width Channels

Figures 7 and 8 illustrate that two types of general pool-riffle morphologies formed within the experimental channel. The first type, referred to as entrainment-driven pool-riffles, occur along channel segments with downstream width variations that proceed from relatively wide segments to narrower ones. The riffle-pool from station 10 to 6 m of the experimental channel reflects an entrainment-driven feature (Figures 7 and 8). The second type, referred to as depositional-driven pool-riffles, is the sequential inverse of the entrainment-driven type, whereby width is organized to proceed from relatively narrow segments to wider ones. The pool-riffle from stations 12 to 10, and 5 to 3 m reflects depositional-driven features (Figure 7). Whereas the discussion here is focused on the apparent role of channel width variation in promoting pool-riffle development, other similar mechanisms exist. For example, pool scour via streamside or within channel physical obstructions (e.g., Buffington et al., 2002; Hawkins et al., 1993; Lisle, 1986), and pool development via downstream damming across some portion of the channel width (e.g., Hawkins et al., 1993).

The names of each pool-riffle type convey the dominant processes responsible for formation. In the first case, entrainment-driven riffle-pools form as a consequence of locally significant rates of net particle entrainment, which yields a pool. Higher than average entrainment rates and pool creation are due to the combination of a narrowing channel section and accelerating flow, coupled with a relatively high upstream riffle water surface elevation. The locally high riffle water surface elevation represents stored PE, which is subsequently converted to KE as flow moves downstream, driving pool formation. The magnitude of topographic difference from riffle to downstream pool is controlled by $\Delta w(x)$, which manifests through associated variations of the water surface slope. Flow entering the upstream riffle and relatively wide segment has a flatter than average water surface slope. Flattening of the water surface slope causes flow to decelerate, promoting net sediment deposition and riffle creation. On the other hand, flow leaving the upstream riffle and entering the downstream pool and relatively narrow segment has a steeper than average water surface slope. Steepening of the water surface slope causes flow to accelerate, promoting net sediment entrainment and pool development. Storage of sediment within the upstream developing riffle may further enhance downstream residual pool depths by depressing the local sediment supply entering the pool during formation (Buffington et al., 2002). Entrainment-driven pool formation is associated with τ/τ_{ref} values well above a value of 2 (Figure 11). The spatial pattern of pool-riffle topography for entrainment-driven structures is captured by the zero-crossing method (Figure 8).

By contrast, depositional-driven pool-riffles form as a consequence of locally significant rates of net particle deposition, which leads to a riffle. Higher than average deposition rates and riffle creation are due to a combination of a widening channel section and decelerating flow. The widening section, decelerating flow, and growing riffle lead to a storage of PE over the upstream part of the riffle, which manifests as locally elevated water surface elevations. Elevated riffle water surface elevations drive locally flatter than average water surface slopes. Channel segments immediately upstream of the points of widening are accordingly back flooded, resulting in a pool. The magnitude of topographic difference from pool to downstream riffle is controlled by $\Delta w(x)$. The shape of the local profile within the upstream pool can be further accentuated through sediment entrainment processes commonly observed in association with instream sills and small run of the river dams, which are commonly associated with enhanced bed erosion within the upstream backwater pool. Depositional-driven pool formation is associated with τ/τ_{ref} values close to critical (Figure 11). The spatial pattern of pool-riffle topography for depositional-driven structures is more subtle, and required use of both the zero-crossing and residual depth methods to identify the structures (Figure 8). Furthermore, Figure 8 illustrates that pool bed slopes for depositional-driven structures are similar, or slightly steeper than the overall longitudinal bed slope. This suggests that net particle entrainment may play a minor role in pool-riffle formation under depositionally driven processes versus entrainment driven. de Almeida and Rodríguez (2011) also reports the prevalence of backwater-controlled pool-riffles for their Bear River, AR, USA, simulation reach.

It is important to identify the different processes that are associated with pool-riffle development for at least two reasons. First, formative hypotheses must account for the development mechanisms required to explain the observations in Figures 7, 8, 11, and 14. The second practical reason is that river restoration practitioners should be aware that different design approaches will yield pool-riffles but that the associated structures will exhibit differing characteristics. We are presently working to examine these issues in more detail.

7. Conclusions and Next Steps

This study provides a theoretical and experimental examination of how the local streamwise bed slope S_{local} within gravel bed streams is coupled to changes of channel width $\Delta w(x)$. We find that S_{local} for five different data sets representing field, numerical, and experimental studies can be reasonably explained by a mathematical model built from simplifying assumptions of uniform flow and statistical steady state conditions. The model states that S_{local} is specifically explained by the product of two terms: Λ and ΔU_x^*. Λ is the ratio of the flow and yielding timescales, which depends on a demonstrated negative covariation between u_* and w for $-0.3 \leq \Delta w(x) \leq +0.5$, assuming a uniform D_{90} grain size and bed surface sediment packing condition ε. ΔU_x^* is a dimensionless velocity, which depends on how the cross-sectionally averaged velocity $\bar{U}_x$ and flow depth $\bar{d}$ vary with changes of channel width. Λ sets the magnitude of S_{local}, and ΔU_x^* determines whether the bed slope is positive or negative. The tested data sets have a range of reach-averaged bed slopes from approximately 0.0001 – 0.015. This result highlights that the proposed mathematical model captures the general physics responsible for development of S_{local}. An important next step is to explore Λ and ΔU_x^* for a wider range of physical conditions, such as differing sediment supply compositions, hydrologic regimes, and flow field characteristics. We develop our scaling expression for S_{local} in terms of the cross-sectionally averaged flow velocity, which simplifies the flow forcing which contributes to the streamwise bed profiles reported herein for PRE1. It may be useful to expand on this perspective and examine whether further insights are gained by considering the turbulent character of the local flow (cf. Legleiter et al., 2011; MacVicar & Roy, 2007a, 2007b).

Comparison between the mathematical model and the tested data sets permits tentative identification of $\Delta w(x)$ thresholds which correlate with development of general pool-riffle bed morphology: $\Delta w(x) = -0.10$ and $+0.10$, respectively. The proposed $\Delta w(x)$ threshold conditions highlight that relatively straight channel segments constrained by $-0.10 < \Delta w(x) < +0.10$ are unlikely to develop pool-riffle pairs, unless they are driven by some other external condition which leads to relatively large spatial differences in sediment transport. For example, development of a partial-span large wood structure. This proposal and finding raises the expectation that the spacing between adjacent pool-riffle pairs in mountain channels with downstream width variation is governed by the spatial character of width variations above the $\Delta w(x)$ thresholds (Repetto et al., 2002). Furthermore, we suggest that pool-riffle formation is the result of at least two different processes: entrainment driven and depositional driven. Which one ultimately governs local conditions depends on the spatial organization of channel width. Therefore, along relatively straight channel segments, the spatial organization of channel width drives the general topographic response. Factors such as bedrock outcrops, instream wood, impinging landslide deposits, and flood-driven processes are all plausible explanations for local width variations. These potentially important local factors taken together expand the mechanics-based pool-riffle formation perspectives presented here, which are based on our simplified experimental setup and theoretical development. An improved and broadened understanding of the processes and factors which can explain pool-riffle formation has important implications for stream restoration and enhancement projects. Applied projects benefit from a reduction in design risk, which is typically due to evolutionary uncertainties associated with constructed conditions that cannot be adequately anticipated. We are presently working to address this risk issue, motivated by the findings of this study.

Notation

A The flow area L^2
$\bar{d}$ The average flow depth L
D_g Geometric mean grain size L
D_{gf} Geometric mean grain size of the upstream sediment supply L
D_{gs} Geometric mean grain size of the bed surface L
D'_g D_{gs}/D_{gf} (-)
D_i Characteristic grain size of the bed surface L
D_{50} 50th percentile grain size L
D_{90} 90th percentile grain size L
D_{90f} 90th percentile grain size of the upstream sediment supply L
D_{90s} 90th percentile grain size of the bed surface L
D'_{90} D_{90s}/D_{90f} (-)
g Acceleration due to gravity LT^{-2}

L_a Active layer thickness of bedload transported by the flow L
L_c Characteristic length scale L
k Scaling constant (-)
k_s Measure of local bed roughness: $n_k D_{90} L$
n_k Dimensionless scaling constant ≈ 2 (-)
q_b Total bedload sediment transport rate L^2T
q_b^* Dimensionless total bedload sediment transport rate (-)
q_w Unit discharge: Q_w/wL^2T
Q_{sf} The sediment flux MT^{-1}
$\bar{Q}_{sf}$ The average sediment flux MT^{-1}
Q_{ss} The sediment supply rate MT^{-1}
Q_w The water flow rate L^3T^{-1}
S Average local water surface slope (-)
S_b Reach-averaged bed surface slope (-)
S_{local} Local bed slope (-)
t_a The activation time T
t_e The elapsed time T
t_f Flow forcing timescale T
t_o t_e/t_a (-)
t_y Particle yielding timescale T
u_* Shear velocity LT^{-1}
U_c Characteristic velocity scale LT^{-1}
$\bar{U}_x$ Downstream cross-sectionally averaged flow velocity LT^{-1}
$\hat{U}_x$ Normalized downstream cross-sectionally averaged flow velocity (-)
$\bar{U}_x^*$ Nondimensional velocity scale; see equation (9) (-)
w Channel width L
$\bar{w}$ Average channel width L
$\Delta w(x)$ Fractional width change as a forward difference with the origin at the downstream end (-)
x Channel station L
Δx Forward difference length scale L
α_r Dimensionless constant equal to 8.1 (-)
$\Delta\tilde{\alpha}$ Downstream change in the average local width to flow depth ratio (-)
ε Solid fraction of the bed (-)
η Bed elevation L
η' Normalized average bed elevation (-)
$\bar{\eta}'$ Normalized average bed elevation for the 12 subsampling locations (-)
λ Downstream spacing between sequential pools or riffles L
Λ Ratio of bed topography spreading to flow forcing timescales (-)
ν The kinematic viscosity of water L^2T
ρ_w Density of water ML^3
ρ' $(\rho_w/\rho_s) - 1$ (-)
ρ_s Density of sediment ML^3
τ The average bed stress $ML^{-1}T^{-2}$
$\tau*$ Dimensionless bed stress, referred to as "particle mobility" (-)
$\hat{\tau}^*$ Normalized dimensionless bed stress, referred to as "particle mobility" (-)
$\tau^*_{c_{50}}$ The reference dimensionless critical bed stress for the D_{50} (-)
τ_{ref} The reference average critical bed stress $ML^{-1}T^{-2}$
τ^*_{ref} Equivalent to $\tau^*_{c_{50}}$ (-)
ϕ Volume-averaged streambed porosity (-)
χ Scaling factor (-)

Acknowledgments
S. M. C. received funding from an Alexander Graham Bell Canada Graduate Scholarship awarded from the National Sciences and Engineering Research Council Canada, and a Mitacs Accelerate Program Fellowship. Flume experiments were generously supported by an NSERC Discovery grant, and a Canada Foundation for Innovation grant to M. H. Support for A. M. J. was provided through an NSERC Discovery grant. S. M. C. appreciates insightful discussions with John Buffington, Paul Carling, Tom Dunne, and in particular, David Furbish, who helped to motivate some of the directions pursued during the work, and whose support has been very helpful. Review of an earlier version of the manuscript by Tom Dunne helped to improve the presentation of the material, as well as the focus. The authors also thank the Associate Editor Bruce MacVicar, the Editor John Buffington, and two anonymous reviewers for insightful, constructive, and overall excellent reviews, which were instrumental in shaping the final version of this paper. The authors report no financial conflicts of interest in completing this work or preparing this manuscript. Data used in preparation of this manuscript can be downloaded from https://doi.org/10.17632/zmjvt32gj3.3 (Chartrand et al., 2017).

References

Acreman, M., Arthington, A. H., Colloff, M. J., Couch, C., Crossman, N. D., Dyer, F., et al. (2014). Environmental flows for natural, hybrid, and novel riverine ecosystems in a changing world. *Frontiers in Ecology and the Environment*, *12*(8), 466–473. https://doi.org/10.1890/130134

Acreman, M. C., Overton, I. C., King, J., Wood, P. J., Cowx, I. G., Dunbar, M. J., et al. (2014). The changing role of ecohydrological science in guiding environmental flows. *Hydrological Sciences Journal*, *59*(3-4), 433–450. https://doi.org/10.1080/02626667.2014.886019

Ancey, C. (2010). Stochastic modeling in sediment dynamics: Exner equation for planar bed incipient bed load transport conditions. *Journal of Geophysical Research*, *115*, F00A11. https://doi.org/10.1029/2009JF001260

Bayat, E., Rodríguez, J. F., Saco, P. M., de Almeida, G. A. M., Vahidi, E., & García, M. H. (2017). A tale of two riffles: Using multidimensional, multifractional, time-varying sediment transport to assess self-maintenance in pool-riffle sequences. *Water Resources Research*, *53*, 2095–2113. https://doi.org/10.1002/2016WR019464

Beechie, T. J., & Sibley, T. H. (1997). Relationships between channel characteristics, woody debris, and fish habitat in northwestern Washington streams. *Transactions of the American Fisheries Society*, *126*(2), 217–229. https://doi.org/10.1577/1548-8659(1997)126<0217:RBCCWD>2.3.CO;2

Blom, A., Arkesteijn, L., Chavarrías, V., & Viparelli, E. (2017). The equilibrium alluvial river under variable flow and its channel-forming discharge. *Journal of Geophysical Research: Earth Surface*, *122*, 1924–1948. https://doi.org/10.1002/2017JF004213

Blom, A., Viparelli, E., & Chavarrías, V. (2016). The graded alluvial river: Profile concavity and downstream fining. *Geophysical Research Letters*, *43*, 6285–6293. https://doi.org/10.1002/2016GL068898

Bolla Pittaluga, M., Luchi, R., & Seminara, G. (2014). On the equilibrium profile of river beds. *Journal of Geophysical Research: Earth Surface*, *119*, 317–332. https://doi.org/10.1002/2013JF002806

Booker, D., Sear, D., & Payne, A. (2001). Modelling three-dimensional flow structures and patterns of boundary shear stress in a natural pool-riffle sequence. *Earth Surface Processes and Landforms*, *26*(5), 553–576. https://doi.org/10.1002/esp.210

Brown, R. A., & Pasternack, G. B. (2017). Bed and width oscillations form coherent patterns in a partially confined, regulated gravel–cobble-bedded river adjusting to anthropogenic disturbances. *Earth Surface Dynamics*, *5*(1), 1–20. https://doi.org/10.5194/esurf-5-1-2017

Buffington, J. M., Lisle, T. E., Woodsmith, R. D., & Hilton, S. (2002). Controls on the size and occurrence of pools in coarse-grained forest rivers. *River Research and Applications*, *18*(6), 507–531. https://doi.org/10.1002/rra.693

Caamaño, D., Goodwin, P., Buffington, J., Liou, J., & Daley-Laursen, S. (2009). Unifying criterion for the velocity reversal hypothesis in gravel-bed rivers. *Journal of Hydraulic Engineering*, *135*(1), 66–70. https://doi.org/10.1061/(ASCE)0733-9429(2009)135:1(66)

Cao, Z., Carling, P., & Oakey, R. (2003). Flow reversal over a natural pool-riffle sequence: A computational study. *Earth Surface Processes and Landforms*, *28*(7), 689–705. https://doi.org/10.1002/esp.466

Carling, P. (1991). An appraisal of the velocity-reversal hypothesis for stable pool-riffle sequences in the river Severn, England. *Earth Surface Processes and Landforms*, *16*(1), 19–31. https://doi.org/10.1002/esp.3290160104

Carling, P., & Orr, H. (2000). Morphology of riffle-pool sequences in the River Severn, England. *Earth Surface Processes and Landforms*, *25*(4), 369–384.

Carling, P., & Wood, N. (1994). Simulation of flow over pool-riffle topography: A consideration of the velocity reversal hypothesis. *Earth Surface Processes and Landforms*, *19*(4), 319–332. https://doi.org/10.1002/esp.3290190404

Chartrand, S., Jellinek, A., Hassan, M., & Ferrer-Boix, C. (2017). Experimental data set for morphodyanmics of a width-variable gravel-bed stream: New insights on pool-riffle formation. Mendeley Data. https://10.17632/zmjvt32gj3.3

Chartrand, S. M., & Whiting, P. J. (2000). Alluvial architecture in headwater streams with special emphasis on step-pool topography. *Earth Surface Processes and Landforms*, *25*, 583–600. https://doi.org/10.1002/1096-9837(200006)25:6<583::AID-ESP92>3.0.CO;2-3

Church, M., Hassan, M. A., & Wolcott, J. F. (1998). Stabilizing self-organized structures in gravel-bed stream channels: Field and experimental observations. *Water Resources Research*, *34*(11), 3169–3179. https://doi.org/10.1029/98WR00484

Church, M., & Jones, D. (1982). Channel bars in gravel-bed rivers. In R. D. Hey, J. C. Bathurst, & C.R. Thorne (Eds.), *Gravel-bed rivers* (pp. 291–338). Chichester, UK: John Wiley.

Clifford, N. (1993). Formation of riffle-pool sequences: Field evidence for an autogenetic process. *Sedimentary Geology*, *85*(1-4), 39–51.

de Almeida, G. A. M., & Rodríguez, J. F. (2011). Understanding pool-riffle dynamics through continuous morphological simulations. *Water Resources Research*, *47*, W01502. https://doi.org/10.1029/2010WR009170

de Almeida, G. A. M., & Rodríguez, J. F. (2012). Spontaneous formation and degradation of pool-riffle morphology and sediment sorting using a simple fractional transport model. *Geophysical Research Letters*, *39*, L06407. https://doi.org/10.1029/2012GL051059

Dolan, R., Howard, A., & Trimble, D. (1978). Structural control of the rapids and pools of the Colorado River in the Grand Canyon. *Science (New York N.Y.)*, *202*(4368), 629–31. https://doi.org/10.1126/science.202.4368.629

Duró, G., Crosato, A., & Tassi, P. (2016). Numerical study on river bar response to spatial variations of channel width. *Advances in Water Resources, Part A*, *93*, 21–38. https://doi.org/10.1016/j.advwatres.2015.10.003

Eaton, B. C., Church, M., & Davies, T. R. H. (2006). A conceptual model for meander initiation in bedload-dominated streams. *Earth Surface Processes and Landforms*, *31*(7), 875–891. https://doi.org/10.1002/esp.1297

Einstein, H. A (1950). *The bed-load function for sediment transportation in open channel flows*. Washington, D. C.: USDA Soil Conservation Service Technical Bulletin 1026 U.S. Department of Agriculture.

Emmett, W. W. (1999). Quantification of channel-maintenance flows for gravel-bed rivers. In D. Olsen & J. P. Potyondy (Eds.), *Hydrology, wildland* (pp. 77–84). Herndon, VA: American Water Resources Association.

Exner, F. (1925). Uber die Wechselwirkung zwischen Wasser und Geschiebe in ussen, Sitzungber. *Sitzungs Bericht Akad Wiss. Wien. Abt.*, *2a*, 165–203.

Fathel, S. L., Furbish, D. J., & Schmeeckle, M. W. (2015). Experimental evidence of statistical ensemble behavior in bed load sediment transport. *Journal of Geophysical Research: Earth Surface*, *120*, 2298–2317. https://doi.org/10.1002/2015JF003552

Ferrer-Boix, C., Chartrand, S. M., Hassan, M. A., Martín-Vide, J. P., & Parker, G. (2016). On how spatial variations of channel width influence river profile curvature. *Geophysical Research Letters*, *43*, 6313–6323. https://doi.org/10.1002/2016GL069824

Ferrer-Boix, C., & Hassan, M. A. (2014). Influence of the sediment supply texture on morphological adjustments in gravel-bed rivers. *Water Resources Research*, *50*, 8868–8890. https://doi.org/10.1002/2013WR015117

Furbish, D. J. (1998). Irregular bed forms in steep, rough channels: 1. Stability analysis. *Water Resources Research*, *34*(12), 3635–3648. https://doi.org/10.1029/98WR02339

Furbish, D. J., Thorne, S. D., Byrd, T. C., Warburton, J., Cudney, J. J., & Handel, R. W. (1998). Irregular bed forms in steep, rough channels: 2. Field observations. *Water Resources Research*, *34*(12), 3649–3659. https://doi.org/10.1029/98WR02338

Harrison, L., & Keller, E. (2007). Modeling forced pool-riffle hydraulics in a boulder-bed stream, Southern California. *Geomorphology*, *83*(3-4), 232–248. https://doi.org/10.1016/j.geomorph.2006.02.024

Hassan, M. A., Smith, B. J., Hogan, D. L., Luzi, S. L., David, A. E., Zimmerman, A. E., & Eaton, B. C. (2008). Sediment storage and transport in coarse bed streams: Scale considerations. In H. Habersack, H. Piegay, & M. Rinaldi (Eds.), *Gravel-bed rivers VI: From process understanding to river restoration* (pp. 473–496). Amsterdam: Elsevier. https://doi.org/10.1016/S0928-2025(07)11137-8

Hassan, M. A., & Woodsmith, R. D. (2004). Bed load transport in an obstruction-formed pool in a forest, gravelbed stream. *Geomorphology*, *58*(1), 203–221. https://doi.org/10.1016/j.geomorph.2003.07.006

Hawkins, C. P., Kershner, J. L., Bisson, P. A., Bryant, M. D., Decker, L. M., Gregory, S. V., et al. (1993). A hierarchical approach to classifying stream habitat features. *Fisheries*, *18*(6), 3–12. https://doi.org/10.1577/1548-8446(1993)018<0003:AHATCS>2.0.CO;2

Henderson, F. M. (1966). *Open Channel Flow*, Macmillan series in civil engineering (pp. 522). New York: Macmillan.

Hirano, M. (1971). River-bed degradation with armoring. *Proceedings of the Japan Society of Civil Engineers*, *1971*(3), 55–65.

Hodge, R., Sear, D., & Leyland, J. (2012). Spatial variations in surface sediment structure in riffle-pool sequences: A preliminary test of the differential sediment entrainment hypothesis (DSEH). *Earth Surface Processes and Landforms*, *38*(5), 449–465. https://doi.org/10.1002/esp3290

Juez, C., Ferrer-Boix, C., Murillo, J., Hassan, M. A., & García-Navarro, P. (2016). A model based on Hirano-Exner equations for two-dimensional transient flows over heterogeneous erodible beds. *Advances in Water Resources*, *87*, 1–18. https://doi.org/10.1016/j.advwatres.2015.10.013

Keller, E. (1969). Form and fluvial processes of dry creek, near winters, California (Ph.D Thesis), Davis.

Keller, E. A. (1971). Areal sorting of bed-load material: The hypothesis of velocity reversal. *Geological Society of America Bulletin*, *82*(3), 753.

Keller, E. A., & Melhorn, W. N. (1978). Rhythmic spacing and origin of pools and riffles. *Geological Society of America Bulletin*, *89*(5), 723.

Leeder, M. R. (1982). *Transport of sediment grains — Sedimentology: Process and product* (pp. 67–75). Netherlands, Dordrecht: Springer. https://doi.org/10.1007/978-94-009-5986-6

Legleiter, C. J., Harrison, L. R., & Dunne, T. (2011). Effect of point bar development on the local force balance governing flow in a simple, meandering gravel bed river. *Journal of Geophysical Research*, *116*(1). https://doi.org/10.1029/2010JF001838

Leopold, L., & Wolman, M. G. (1957). River channel patterns: Braided, meandering, and straight, United States Geological Survey Professional Paper 282-B. Washington, D.C.: U.S. Government Printing Office.

Leopold, L. B., Wolman, M. G., & Miller, J. P. (1964). *Fluvial processes in geomorphology*. New York, NY: Dover Publications, Inc.

Lisle, T. E. (1979). A sorting mechanism for a riffle-pool sequence. *Geological Society of America Bulletin*, *90*(7), 1142–1157.

Lisle, T. E. (1986). Stabilization of a gravel channel by large streamside obstructions and bedrock bends, Jacoby Creek, northwestern California. *Geological Society of America Bulletin*, *97*(8), 999–1011.

MacKenzie, L. G., & Eaton, B. C. (2017). Large grains matter: Contrasting bed stability and morphodynamics during two nearly identical experiments. *Earth Surface Processes and Landforms*, *42*, 1287–1295. https://doi.org/10.1002/esp.4122

Mackin, J. (1948)Concept of the graded river. *Geological Society of America Bulletin*, *59*(5), 463–512. https://doi.org/10.1130/0016-7606(1948)59[463:COTGR]2.0.CO;2

MacVicar, B., & Best, J. (2013). A flume experiment on the effect of channel width on the perturbation and recovery of flow in straight pools and riffles with smooth boundaries. *Journal of Geophysical Research: Earth Surface*, *118*, 1850–1863. https://doi.org/10.1002/jgrf.20133

MacVicar, B., Obach, L., & Best, J. (2013). Large-scale coherent flow structures in alluvial pools. In J. Venditti, J. Best, M. Church, & R. Hardy (Eds.), *Coherent flow structures at Earth's surface* (pp. 243–259). Chichester, UK: John Wiley. https://doi.org/10.1002/9781118527221.ch16

MacVicar, B., & Rennie, C. (2012). Flow and turbulence redistribution in a straight artificial pool. *Water Resources Research*, *48*, W02503. https://doi.org/10.1029/2010WR009374

MacVicar, B., & Roy, A. G. (2007a). Hydrodynamics of a forced riffle pool in a gravel bed river: 1. Mean velocity and turbulence intensity. *Water Resources Research*, *43*, W12401. https://doi.org/10.1029/2006WR005272

MacVicar, B., & Roy, A. G. (2007b). Hydrodynamics of a forced riffle pool in a gravel bed river: 2. Scale and structure of coherent turbulent events. *Water Resources Research*, *43*, W12402. https://doi.org/10.1029/2006WR005274

MacWilliams, M., Wheaton, J., Pasternack, G., Street, R., & Kitanidis, P. (2006). Flow convergence routing hypothesis for pool-riffle maintenance in alluvial rivers. *Water Resources Research*, *42*, W10427. https://doi.org/10.1029/2005WR004391

Massey, F. (1951). The Kolmogorov-Smirnov test for goodness of fit. *Journal of the American Statistical Association*, *46*(253), 68–78. https://doi.org/10.1080/01621459.1951.10500769

Masteller, C. C., & Finnegan, N. J. (2017). Interplay between grain protrusion and sediment entrainment in an experimental flume. *Journal of Geophysical Research: Earth Surface*, *122*, 274–289. https://doi.org/10.1002/2016JF003943

Melton, M. A. (1962). Methods for measuring the effect of environmental factors on channel properties. *Journal of Geophysical Research*, *67*(4), 1485–1490. https://doi.org/10.1029/JZ067i004p01485

Milan, D. (2000). Sand and gravel transport through a riffle-pool sequence (Ph.D. thesis), Newcastle University.

Montgomery, D. R., & Buffington, J. M. (1997). Channel-reach morphology in mountain drainage basins. *Geological Society of America Bulletin*, *109*(5), 596–611. https://doi.org/10.1130/0016-7606(1997)109

Montgomery, D. R., Buffington, J. M., Smith, R. D., Schmidt, K. M., & Pess, G. (1995). Pool spacing in forest channels. *Water Resources Research*, *31*(4), 1097–1105. https://doi.org/10.1029/94WR03285

Nelson, P., Brew, A. K., & Morgan, J. A. (2015). Morphodynamic response of a variable-width channel to changes in sediment supply. *Water Resources Research*, *51*, 5717–5734. https://doi.org/10.1002/2014WR016806

Paola, C., & Mohrig, D. (1996). Palaeohydraulics revisited: Palaeoslope estimation in coarse-grained braided rivers. *Basin Research*, *8*(3), 243–254. https://doi.org/10.1046/j.1365-2117.1996.00253.x

Paola, C., & Voller, V. R. (2005). A generalized Exner equation for sediment mass balance. *Journal of Geophysical Research*, *110*, F04014. https://doi.org/10.1029/2004JF000274

Parker, G. (2007). 1D sediment transport morphodynamics with applications to rivers and turbidity currents.

Parker, G. (2008). Transport of gravel and sediment mixtures. In M. Garcia (Ed.), *Sedimentation engineering: Theory, measurements, modeling and practice (ASCE Manuals and Reports on Engineering Practice No. 110)*, 3. Reston, VA: ASCE, pp. 165–251.

Parker, G., Toro-Escobar, C. M., Ramey, M., & Beck, S. (2003). Effect of floodwater extraction on mountain stream morphology. *Journal of Hydraulic Engineering*, *129*(11), 885–895. https://doi.org/10.1061/(ASCE)0733-9429(2003)129:11(885)

Phillips, C. B., & Jerolmack, D. J. (2016). Self-organization of river channels as a critical filter on climate signals. *Science*, *352*(6286), 694–697. https://doi.org/10.1126/science.aad3348

Pickup, G., & Rieger, W. A. (1979). A conceptual model of the relationship between channel characteristics and discharge. *Earth Surface Processes*, *4*(1), 37–42. https://doi.org/10.1002/esp.3290040104

Poff, N. N., Allan, J. D., Bain, M. B., Karr, J. R., Prestegaard, K. L., Richter, B. D., et al. (1997). The natural flow regime. *BioScience*, *47*(11), 769–784. https://doi.org/10.2307/1313099

Repetto, R., Tubino, M., & Paola, C. (2002). Planimetric instability of channels with variable width. *Journal of Fluid Mechanics*, *457*, 79–109. https://doi.org/10.1017/S0022112001007595

Richards, K. S. (1976a). Channel width and the riffle-pool sequence. *Geological Society of America Bulletin*, *87*(6), 883.

Richards, K. S. (1976b). The morphology of riffle-pool sequences. *Earth Surface Processes and Landforms*, *1*(1), 71–88. https://doi.org/10.1002/esp.3290010108

Rodríguez, J. F., García, C. M., & García, M. H. (2013). Three-dimensional flow in centered pool-riffle sequences. *Water Resources Research*, *49*, 202–215. https://doi.org/10.1029/2011WR011789

Schneider, J. M., Rickenmann, D., Turowski, J. M., Schmid, B., & Kirchner, J. W. (2016). Bed load transport in a very steep mountain stream (Riedbach, Switzerland): Measurement and prediction. *Water Resources Research*, *52*, 9522–9541. https://doi.org/10.1002/2016WR019308

Sear, D. (1996). Sediment transport processes in pool-riffle sequences. *Earth Surface Processes and Landforms*, *21*(3), 241–262. https://doi.org/10.1002/(SICI)1096-9837(199603)21:3<241::AID-ESP623>3.0.CO;2-1

Shields, A. (1936). Anwendung der Ähnlichkeitsmechanik und der Turbulenzforschung auf die Geschiebebewegung. *Mitteilungen der Preussischen Versuchsanstalt für Wasserbau und Schiffbau*, 26 pp.

Slingerland, R., & Kump, L. (2011). *Mathematical modeling of Earth's dynamical systems: A primer* (pp. 231). Princeton, NJ: Princeton University Press.

Snow, R. S., & Slingerland, R. L. (1987). Mathematical modeling of graded river profiles. *The Journal of Geology*, *95*(1), 15–33.

Stecca, G., Siviglia, A., & Blom, A. (2014). Mathematical analysis of the Saint-Venant-Hirano model for mixed-sediment morphodynamics. *Water Resources Research*, *50*, 7563–7589. https://doi.org/10.1002/2014WR015251

Thompson, D. (2001). Random controls on semi-rhythmic spacing of pools and riffles in constriction-dominated rivers. *Earth Surface Processes and Landforms*, *26*(11), 1195–1212. https://doi.org/10.1002/esp.265

Thompson, D. M. (2013). 9.21 pool-riffle. In J. F. Shroder (Ed.), *Treatise on geomorphology*. San Diego: Academic Press (pp. 364–378). https://doi.org/10.1016/B978-0-12-374739-6.00246-3

Thompson, D., & Fixler, S. (2017). Formation and maintenance of a forced pool-riffle couplet following loading of large wood. *Geomorphology*, *296*, 74–90. https://doi.org/10.1016/j.geomorph.2017.08.030

Thompson, D., & McCarrick, C. (2010). A flume experiment on the effect of constriction shape on the formation of forced pools. *Hydrology and Earth System Sciences*, *14*, 1321–1330. https://doi.org/10.5194/hess-14-1321-2010

Thompson, D., Nelson, J. M., & Wohl, E. (1998). Interactions between pool geometry and hydraulics. *Water Resources Research*, *34*(12), 3673–3681. https://doi.org/10.1029/1998WR900004

Thompson, D., Wohl, E., & Jarrett, R. (1999). Velocity reversals and sediment sorting in pools and riffles controlled by channel constrictions. *Geomorphology*, *27*(3-4), 229–241.

Venditti, J. G., Rennie, C. D., Bomhof, J., Bradley, R. W., Little, M., & Church, M. (2014). Flow in bedrock canyons. *Nature*, *513*(7519), 534–537.

Wang, T., & Liu, X. (2009). The breakup of armor layer in a gravel-bed stream with no sediment supply, *Advances in water resources and hydraulic engineering* (pp. 919–923). Berlin, Heidleberg: Springer. https://doi.org/10.1007/978-3-540-89465-0-161

White, J. Q., Pasternack, G. B., & Moir, H. J. (2010). Valley width variation influences riffle-pool location and persistence on a rapidly incising gravel-bed river. *Geomorphology*, *121*(3-4), 206–221. https://doi.org/10.1016/j.geomorph.2010.04.012

Whiting, P., Stamm, J., Moog, D., & Orndorff, R. (1999). Sediment-transporting flows in headwater streams. *Geological Society of America Bulletin*, *111*(3), 450–466. https://doi.org/10.1130/0016-7606(1999)111<0450:STFIHS>2.3.CO;2

Wilcock, P. R., & Crowe, J. C. (2003). Surface-based transport model for mixed-size sediment. *Journal of Hydraulic Engineering*, *129*(2), 120–128. https://doi.org/10.1061/(ASCE)0733-9429(2003)129:2(120)

Wilcock, P. R., & McArdell, B. W. (1997). Partial transport of a sand/gravel sediment. *Water Resources Research*, *33*(1), 235–245. https://doi.org/10.1029/96WR02672

Wilkinson, S. N., Rutherfurd, I. D., & Keller, R. J. (2008). An experimental test of whether bar instability contributes to the formation, periodicity and maintenance of pool-riffle sequences. *Earth Surface Processes and Landforms*, *33*(11), 1742–1756. https://doi.org/10.1002/esp.1645

Williams, G. P. (1978). Bank-full discharge of rivers. *Water Resources Research*, *14*(6), 1141–1154. https://doi.org/10.1029/WR014i006p01141

Wohl, E. E., Vincent, K. R., & Merritts, D. J. (1993). Pool and riffle characteristics in relation to channel gradient. *Geomorphology*, *6*(2), 99–110.

Wolman, M. G., & Miller, J. P. (1960). Magnitude and frequency of forces in geomorphic processes. *The Journal of Geology*, *68*(1), 54–74. https://doi.org/10.1086/626637

Yalin, M. (1971). On the formation of dunes and meanders, *Inproceedings of the 14Th congress of the international association for hydraulic research* pp. C101–108), 3.

Zimmermann, A. E., Church, M., & Hassan, M. A. (2008a). Video-based gravel transport measurements with a flume mounted light table. *Earth Surface Processes and Landforms*, *33*(14), 2285–2296.

Zimmermann, A. E., Church, M., & Hassan, M. A. (2008b). Identification of steps and pools from stream longitudinal profile data. *Geomorphology*, *102*(3), 395–406. https://doi.org/10.1016/j.geomorph.2008.04.009